The emergence of highly fit SARS-CoV-2 variants accelerated by recombination

Michael R. Garvin[1,2+*], Erica T. Prates[1,2+], Jonathon Romero[3], Ashley Cliff [3], Joao Gabriel Felipe Machado Gazolla[1,2], Monica Pickholz[4,5], Mirko Pavicic[1,2], Daniel Jacobson[1,2,*]

Affiliations:

[1]Oak Ridge National Laboratory, Computational Systems Biology, Biosciences, Oak Ridge, TN; [2]National Virtual Biotechnology Laboratory, US Department of Energy; [3]The Bredesen Center for Interdisciplinary Research and Graduate Education, University of Tennessee Knoxville, Knoxville, TN; [4]Departamento de Física, Facultad de Ciencias Exactas y Naturales, Universidad de Buenos Aires, Buenos Aires, Argentina; [5]Instituto de Física de Buenos Aires (IFIBA), CONICET-Universidad de Buenos Aires, Buenos Aires, Argentina.

***Correspondence:** garvinmr@ornl.gov, jacobsonda@ornl.gov

[+]**Contributed equally**

Key words: SARS-CoV-2; recombination; haplotype; Delta variant; variants of concern; COVID-19, syncytia

Running title: Highly fit SARS-CoV-2 generated from recombination

Abstract

The SARS-CoV-2 pandemic has entered an alarming new phase with the emergence of the variants of concern (VOC), P.1, B.1.351, and B.1.1.7, in late 2020, and B.1.427, B.1.429, and B.1.617, in 2021. Substitutions in the spike glycoprotein (S), such as $Asn^{501}Tyr$ and $Glu^{484}Lys$, are likely key in several VOC. However, $Asn^{501}Tyr$ had been circulating for months in earlier strains and $Glu^{484}Lys$ is not found in B.1.1.7, indicating that they do not fully explain those fast-spreading variants. Here we use a computational systems biology approach to process more than 900,000 SARS-CoV-2 genomes and map spatiotemporal relationships, revealing other critical attributes of these variants. Comparisons to earlier dominant mutations and protein structural analyses indicate that the increased transmission is promoted by the combination of functionally complementary mutations in S and in other regions of the SARS-CoV-2 proteome. We report that the VOC have in common mutations in non-S proteins involved in immune-antagonism and replication performance, such as the nonstructural proteins 6 and 13, suggesting a convergent evolution of the virus. Critically, we propose that recombination events among divergent coinfecting haplotypes greatly accelerates the emergence of VOC by bringing together cooperative mutations and explaining the remarkably high mutation load of B.1.1.7. Therefore, extensive community distribution of SARS-CoV-2 increases the probability of future recombination events, further accelerating the evolution of the virus. This study reinforces the need for a global response to stop COVID-19 and future pandemics.

Notice: This manuscript has been authored by UT-Battelle, LLC, under contract DE-AC05-00OR22725 with the US Department of Energy (DOE). The US government retains and the publisher, by accepting the article for publication, acknowledges that the US government retains a nonexclusive, paid-up, irrevocable, worldwide license to publish or reproduce the published form of this manuscript, or allow others to do so, for US government purposes. DOE will provide public access to these results of federally sponsored research in accordance with the DOE Public Access Plan (http://energy.gov/downloads/doe-public-access-plan).

"Nothing in Biology Makes Sense Except in the Light of Evolution" -Theodosius Dobzhansky

1. Introduction

In late 2020, three SARS-CoV-2 variants of concern, VOC; B.1.1.7, B.1.351, and P.1 (also called Alpha, Beta, and Gamma respectively) rapidly became the predominant source of infections due to enhanced transmission rates and have since been linked to increased hospitalizations and mortalities (Alpert et al. 2021; Challen et al. 2021; Faria et al. 2021; Funk et al. 2021; Sabino et al. 2021; Washington et al. 2021; Davies et al.; Volz et al.). In early 2021, several new VOC appeared including, B.1.427 (Epsilon), B.1.526 (Iota), and B.1.617 (Delta). B.1.617 is of immediate concern because it is responsible for the COVID-19 crisis that recently began in India (Singh et al. 2021), is causing the majority of new infections in the United Kingdom (UK), and the United States (USA), and has now been observed in more than 70 countries worldwide. Notably, several of these VOC have rapidly spread even in regions such as the UK that depend on robust sampling efforts for early detection. There is therefore a critical need to identify accurate predictors and biological causes for the increased transmission of the next VOC, which will inevitably emerge if the viral spread is not globally restrained.

Although extensive efforts are underway to achieve these ends, integrating new findings is critical to unravel the multiple biomolecular and environmental factors influencing viral evolution. Toward a holistic understanding of VOC emergence, two major weaknesses need to be addressed: (1) currently, the mutations used to identify VOC and potentially explain the altered biology of the virus are predominantly focused on the changes observed in the spike glycoprotein (S) whereas those in other genomic regions are largely ignored, and (2) the molecular models used to reconstruct the evolutionary history of the virus employ phylogenetic trees that are useful for species-level but not population-based analyses, which is the case with SARS-CoV-2 (Huson and Bryant 2006; Velasco 2013).

For example, the $Asn^{501}Tyr$ substitution in S is likely key because it increases affinity for the host receptor, angiotensin-converting enzyme 2 (ACE2) (Liu et al. 2021), and is often used to identify the late 2020 VOC (Fratev; Luan et al.), but this mutation has been circulating widely at low frequency and only expanded seven months after being first detected. Similarly, the $Glu^{484}Lys$ substitution in S is often discussed in the context of P.1 and B.1.351 VOC and may allow escape from neutralizing antibodies (Starr et al. 2021; Greaney et al.), but is not found in

78 B.1.1.7 and therefore does not explain the increased transmission of all three late 2020 VOC.
79 These characteristics suggest that several mutations including those in S are being transmitted as
80 a linked set, i.e., a haplotype and their combined effects (i.e., epistasis) may be contributing to
81 the rapid viral spread.

82 Widely used molecular evolutionary models based on phylogenetic trees are also
83 problematic because the *algorithms* that are applied assume that mutations appearing in different
84 SARS-CoV-2 haplotypes are due to repeated, independent mutations and the *scientific*
85 *community* is interpreting this as evidence for the same; i.e., the logic is circular. Alternatively,
86 these apparent repeated mutations may represent recombination, which is a common mechanism
87 to accelerate evolution compared to single site mutations in positive strand RNA viruses such as
88 SARS-CoV-2 (Bentley and Evans 2018). Furthermore, phylogenetic trees are unable to
89 incorporate important molecular events and metadata such as geospatial and temporal data that
90 would be highly informative for detecting current and future VOC.

91 In contrast, median-joining networks (MJN) are an efficient and accurate means to
92 analyze haploid genomic data at the population level (Bandelt et al. 1999) such as SARS-CoV-2,
93 (Garvin, Prates, et al. 2020). Unlike independently segregating sites represented in phylogenetic
94 trees, the unit of interest in an MJN is the haplotype, which more accurately reflects the biology
95 of coronaviruses and enables the detection of important evolutionary events such as
96 recombination. Furthermore, a network can be annotated with information including frequency,
97 geospatial location, demographic, or clinical outcomes associated with a unique haplotype to
98 create interpretable patterns of genome variation.

99 Here, we processed more than 900,000 SARS-CoV-2 genomes using a computational
100 workflow that combines MJN and protein structural analysis (Garvin, Prates, et al. 2020; Prates
101 et al. 2020) to identify critical attributes of these VOC and provide substantial evidence that the
102 genome-wide mutation load of the late 2020 VOC results from recombination between divergent
103 strains. Via focused structural analysis and molecular dynamics simulations, we explore the
104 individual effects of key mutations in S and other proteins of SARS-CoV-2 that are shared
105 among different VOC. We propose that linked mutations in VOC act cooperatively to enhance

106 viral spread and our results emphasize the major role of community spread in generating future
107 VOC (Sheikh et al. 2021).

108

109 **2. Results and Discussion**

110 ***Molecular evolution of populations is best represented by a network***

111 The COVID-19 pandemic is both an unprecedented tragedy and an opportunity to study
112 molecular evolution given the abundant and global sampling of the mutational space of SARS-
113 CoV-2. The MJN is a valuable method of integrating these data to understand viral evolution
114 because the model assumes single mutational steps in which each node represents a haplotype
115 and the edge between nodes is a mutation leading to a new one. Typically, a subsample of extant
116 haplotypes for a taxon is obtained and unsampled, or extinct lineages are inferred. In contrast,
117 SARS-CoV-2 sequence data repositories provide extensive sampling of haplotypes and
118 collection dates (the calendar date of the sample). Given that in an MJN, the temporal
119 distribution of haplotypes is inherent (the model assumes time-ordered sets of mutations), the
120 mutational history of the virus can be traced as a genealogy that can incorporate both the relative
121 *and* absolute times of emergence of SARS-CoV-2 variants. Importantly, when the single-
122 mutational step MJN model fails, it produces features such as loops or clusters of inferred
123 haplotypes that can indicate biologically important processes such as recombination events, back
124 mutations, or repeat mutations at a site that may be under positive selection.

125 To make a direct comparison, we generated a network and a phylogenetic tree of SARS-
126 CoV-2 haplotypes that were identified from sequences sampled during the first four months of
127 the pandemic and deposited into GISAID (A Global Initiative on Sharing Avian Flu Data,
128 gisaid.org) (Figure 1). Clearly, important metadata such as haplotype frequency, date of
129 emergence, and mutations of interest are easily displayed on the network but are not on the
130 phylogenetic tree. Likewise, at day 96, reticulations (i.e., homoplasy loops) begin to appear in
131 the MJN, indicating reverse mutations to the ancestral states at specific sites or possibly
132 recombination events that can be explored further. Another important feature identified when
133 using networks, but is lost when using phylogenetic trees, is the presence of polytomies. So-

called soft polytomies often indicate unsampled genomic information at the species level and hard polytomies are molecular events often found in rapidly expanding populations. For example, haplotype H04 in the MJN (Figure 1) represents a hard polytomy and indicates that a frequent variant is further undergoing multiple independent mutational events, but the phylogenetic tree is unable to convey this information.

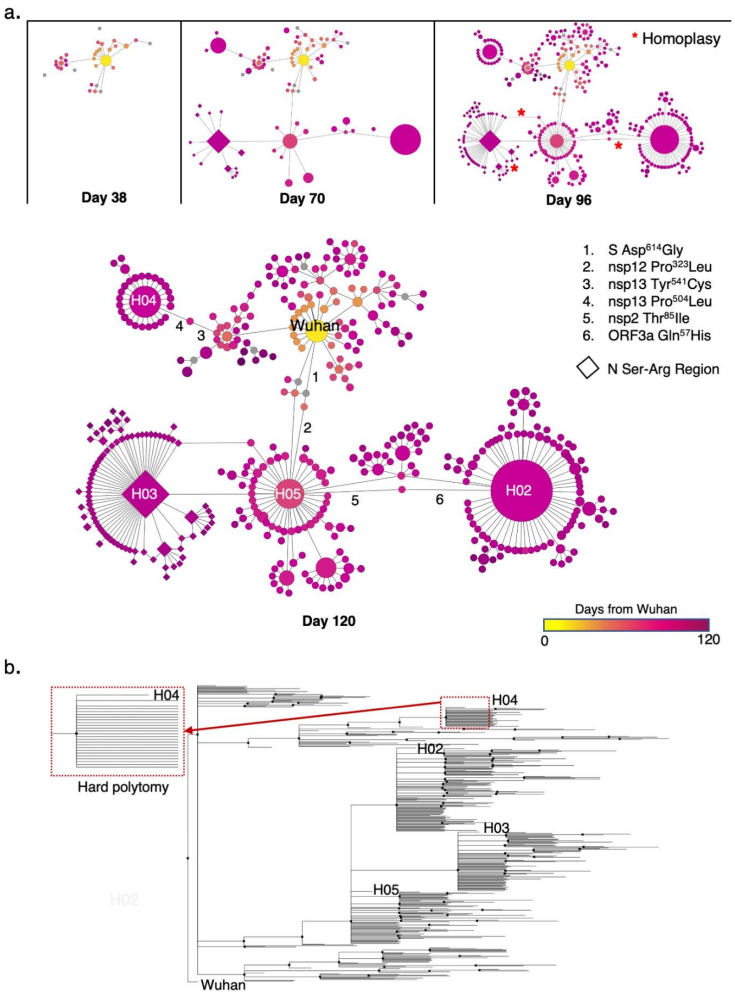

Fig. 1. Comparison of a median-joining network (MJN) and phylogenetic tree generated with SARS-CoV-2 sequences sampled through April 2020. **a**. MJN of SARS-CoV-2 haplotypes, 96, and 120 days. Node sizes in the MJN correspond to sample sizes for a given haplotype and node colors indicate the time of its first report relative to the putative origin of the pandemic in Wuhan. The most abundant haplotypes are named H02 - H05 and numerals 1 - 6 identify important mutations (Garvin, Prates, et al. 2020). Diamond shape nodes denote haplotypes that harbor a 3-bp mutation in the nucleocapsid gene (N) that is highly conserved and directly affects viral replication *in vitro (Tylor et al. 2009; Thorne et al. 2021)*. **b.** The phylogenetic tree is unable to convey the same information. For example, rapidly expanding populations often display polytomies, i.e., single mutations from a common central haplotype. Those events are readily identified on the MJN but difficult to interpret on a tree because they are usually visualized as a multi-pronged fork (outlined in the dashed-line box) rather than a star pattern (compare H04 in (a) and (b)). These true biological processes also cause tree algorithms to perform poorly because they violate their

assumptions, slowing convergence. Additionally, MJN are able to indicate reticulations (i.e., loops) that could denote recombination, reverse mutations, or other biologically important events whereas the forced bifurcation of phylogenetic tree algorithms is unable to display these. Reference sequence: NC_045512, Wuhan, December 24, 2019.

Lineage-defining mutations of Variants of Concern

We processed more than 900,000 SARS-CoV-2 genomes from human and mink, built a MJN network using the 640,211 genomes that survived our quality control workflow, and annotated with PANGO lineages defined in the GISAID database (Figure 2, *see* Methods). This genealogy-based approach to molecular evolution identifies the mutations that define a given haplotype based on the edge between nodes. Here, they define the variants of concern/interest based on the edge that initiates their corresponding clusters of nodes (Table 1).

This approach also enables the identification of all the common features acquired in different VOC, which can elucidate the set of molecular features underlying their rapid spread. For example, the B.1.1.7, B.1.351, and P.1 variants, here referred to as late_2020_VOC, can all be defined by a triple amino acid deletion in the nonstructural protein 6 (nsp6; Ser^{106}_Phe^{108}del) as well as Asn^{501}Tyr in S. Notably this latter mutation has received considerable attention compared to the former (Figure 2a, Table 1), but both are likely key to the biology of these VOC. The MJN also reveals what appears to be a previous dominant but now rare variant (D.2) in Australia; an Ile^{120}Phe mutation in nsp2 was followed immediately by S Ser^{477}Asn, which seems to have led to its rapid expansion in April 2020, indicated by increased node size. This underscores the usefulness of the MJN approach because it is able to convey the sequence of timing of mutational events and the number of individuals carrying those haplotypes simultaneously.

In order to account for sampling bias (there are a disproportionate number of sequences contributed to GISAID by the UK and Australia as well as the high frequency of B.1.1.7 and D.2 in those two geographic locations), we plotted the number of daily samples of selected variants relative to their respective total number of cases to date (April, 2021) and compared the resulting slopes of the linear range of the curves (Figure 2c). The late_2020_VOC, early_2021_VOC, and early_2021_VOI (Table 1) display higher daily accumulation rates, between 1% and 3% of total

observed cases per day, compared to other variants (e.g., B.1.177), which show less than 1% accumulation per day. Notably, the rapid increase in D.2 (2%) supports the MJN view of this as a likely VOC. This analysis and the MJN confirm the importance of monitoring these variants closely and identify both S and non-S mutations that define the current and potential SARS-CoV-2 VOC (Table 1).

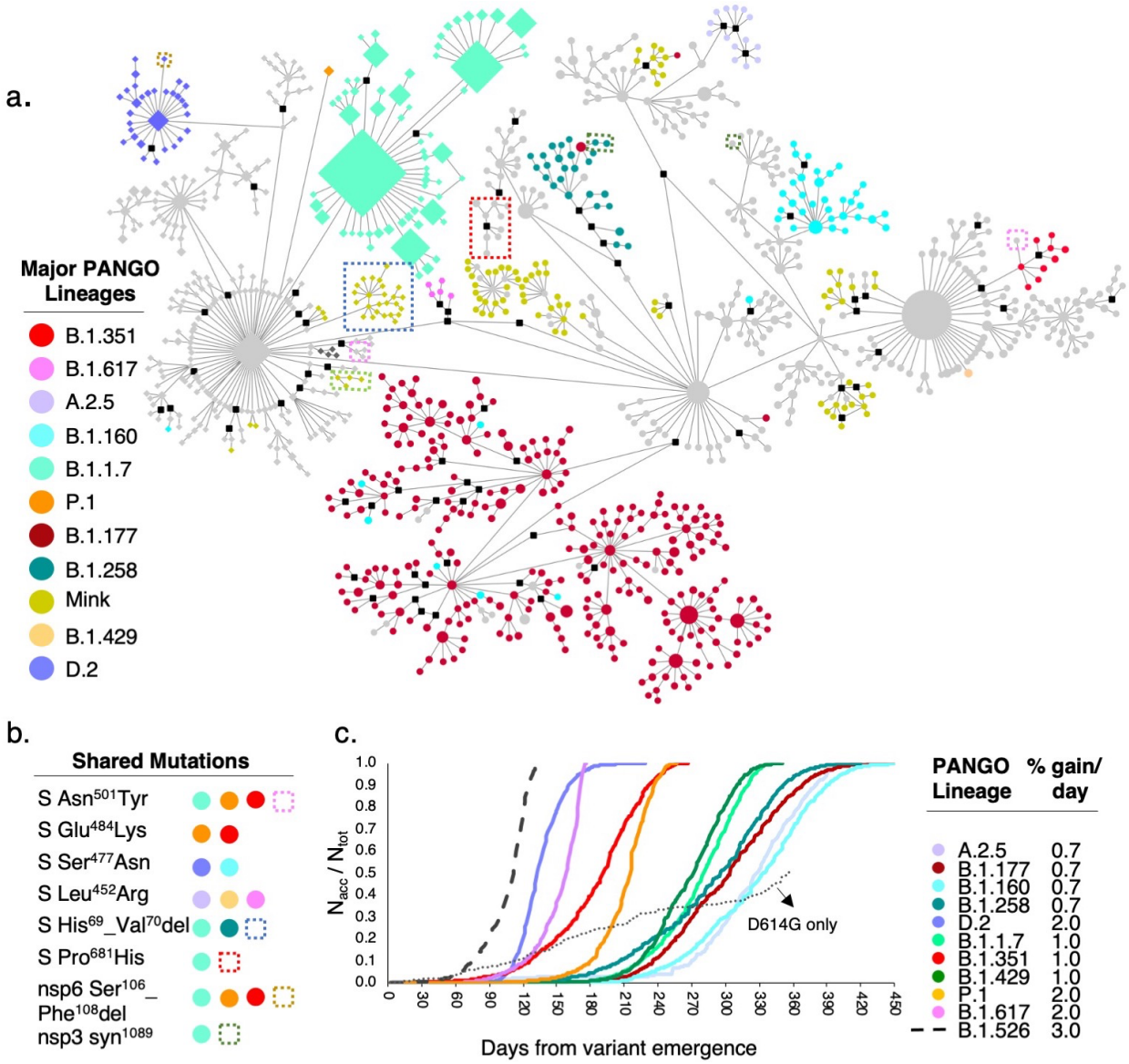

Fig. 2. Median-joining network (MJN) of SARS-CoV-2 genomes. a. MJN of haplotypes found in more than 30 individuals (N=640,211 sequences) using 2,128 variable sites. Colors identify PANGO lineages from GISAID. Diamond-shaped nodes correspond to haplotypes carrying a three base pair deletion in the nucleocapsid gene (N) at sites 28881-28883 ($Arg^{203}Lys$, $Gly^{203}Arg$). Black square nodes are inferred haplotypes, dashed-line box defines a subgroup of haplotypes within a lineage with a disjoint mutation that is also found in B.1.1.7. Several lineages show introgression from others (e.g., cyan nodes, B.1.160, into brick red, B.1.177). **b.** Several important mutations in S and non-S proteins appear in multiple lineages. For example, the B.1.1.7 variant carries four mutations that are in

194 disjoint nodes: S Asn^{501}Tyr, S Pro^{681}His, a silent mutation in the codon for amino acid 1089 in nsp3, and the S
195 His^{69}_Val^{70}del that is also found in a clade of haplotypes from mink (blue dashed-line box in (a)). **c.** Accumulation
196 rate for common GISAID lineages including VOC represented by the ratio between the accumulated number of
197 reported sequences of a given lineage per day since the appearance of that haplotype (N_{acc}) divided by the
198 corresponding total number (N_{tot}) at the final sample date for this study. Colors of curves correspond to node colors
199 in (a). All VOC display accumulation rates of at least 1% of the total for that variant per day. The remaining are
200 less than 1% except for the VOI B.1.526 (not displayed in MJN) that is the highest with 3% per day, indicating
201 further scrutiny of this variant is warranted. We also plotted the accumulation rate for lineages that carry the widely
202 reported S Asp^{614}Gly mutation but without the nsp12 Pro^{323}Leu commonly found with it, supporting our previous
203 hypothesis (Garvin, Prates, et al. 2020) that mutations in S alone are not responsible for the rapid transmission of
204 these VOC/VOI but is a function of epistasis among S and non-S mutations. Reference sequence: NC_045512,
205 Wuhan, December 24, 2019.

206

207 **Table 1. Major lineages shown in the median-joining network and their defining mutations**. Center for disease
208 control (CDC)-defined variants and their timing are listed under *Lineages* and discussed in the text. L-VOC denotes
209 likely variants of concern, that is, those that we propose to have strong potential to become VOC. Non-VOC (N-
210 VOC) are not identified by CDC as VOC. Potential epistatic non-S mutations lineage-defining mutations are listed
211 for the VOC, L-VOC, and VOI. Sites in red font are discussed in the text.

Lineage	Class	Spike Mutation(s)	Likely non-S Epistatic Partner(s)	First major detection
B.1	Early_2020_VOC	D614G	nsp12 P323L	Germany
B.1.1.7 (alpha)	Late_2020_VOC	N501Y, del 69-70, P681H*, T716I,D1118H	nsp6 del 106-108, N L3D, N S235Y	United Kingdom
B.1.351 (beta)	Late_2020_VOC	N501Y, E484K, K417N	nsp6 del 106-108	South Africa
P.1 (gamma)	Late_2020_VOC	N501Y, E484K, K417N	nsp6 del 106-108	Brazil
B.1.427 (epsilon)	Early_2021_VOC	L452R, S13I	nsp13 D260Y	United States, California
B.1.429	Early_2021_VOC	L452R, W152C	nsp13 D260Y	United States, Washington
B.1.617 (delta)	Early_2021_VOC	L452R, E484Q, P681R*	N R203M, ORF7a V82G, ORF3a S26L	India
A.2.5	L-VOC	L452R, del 142-145	nsp1 L4P, nsp3 K839E, nsp4 P308Y	Panama
D.2	L-VOC	S477N	nsp2 I120F	Australia
B.1.160	N-VOC	S477N	na	Denmark
B.1.177	N-VOC	A222V	na	United Kingdom/Denmark
B.1.258	N-VOC	N434K, del 69-70	na	Denmark
B.1.526 (iota)	Early_2021_VOI	L5P, T95I, D253G	nsp6 del 106-108, nsp4 L438P, nsp13 Q88H	United States, New York

212 * multibasic furin cleavage site

213

214 ***Recombination is the likely source for the rapidly expanding variants***

215 Haploid, clonally replicating organisms such as SARS-CoV-2 are predicted to eventually
216 become extinct due to the accumulation of numerous slightly deleterious mutations over time,
217 i.e., Muller's ratchet (Muller 1964). Recombination is not only a rescue from Muller's ratchet, it
218 can also accelerate evolution by allowing for the union of advantageous mutations from
219 divergent haplotypes (Bentley and Evans 2018). In SARS-CoV-2, recombination manifests as a
220 template switch during replication when more than one haplotype is present in the host cell, i.e.
221 the virus replisome stops processing a first RNA strand and switches to a second one from a
222 different haplotype, producing a hybrid virus (Simon-Loriere and Holmes 2011). In fact,

223 template switching is a necessary step during the negative-strand synthesis of SARS-CoV-2
224 when the replisomes functions as an RNA-dependent RNA polymerase and pauses at
225 transcription-regulatory motifs of the sub-genomic template to add the leader sequence from the
226 5' end of the genome (this "recombination" is not detected if only a single strain is present, i.e.
227 there is no variation) (Kim et al. 2020),). Given this and the fact that recombination is a major
228 mechanism of coronavirus evolution (Boni et al. 2020) it would be improbable for this process
229 *not* to occur in the case of multiple strains infecting a cell (Gribble et al. 2021).

230 The late_2020_VOC exhibits large numbers of new mutations relative to any closely
231 related sequence indicating rapid evolution of SARS-CoV-2 (Figure 3a). For example, the
232 original node of B.1.1.7 differs from the most closely related node by 28 mutations. However,
233 the majority of this total (15) corresponds to deletions that could be considered two single
234 mutational events, as does a 3-bp change in N (28280-22883) since they occur in factors of three
235 (a codon), maintaining the coding frame. By summing the two deletions and the full codon
236 change 3-bp change in N with the 10 remaining single site mutations, a conservative estimate
237 would be 13 distinct mutational events leading to B.1.1.7. The plot of the accumulating
238 mutations in the 640,211 haplotypes sampled to date reveals a linear growth of roughly 0.05
239 mutations per day (Figure 3b) and therefore, given this pace, it would be expected to take 260
240 days for these 13 mutational events to accumulate in a haplotype. For the B.1.1.7 to appear in
241 October 2020 as reported, the genealogy would have to have been initiated in January 2020 and
242 yet the nearest node harboring the S Asn^{501}Tyr mutation was not sampled until June 2020 and no
243 intermediate haplotypes have been identified to date.

244 Alternatively, it could be that the 13 mutational events occurred between June and
245 October (122 days), but the probability of this is about one in 10^{15} (Supplemental Methods).
246 Furthermore, all 28 differences between the Wuhan reference sequence and B.1.1.7 appeared in
247 earlier haplotypes (Table S1) and therefore, if rapid evolution were the cause, it would require
248 the extremely unlikely process of 28 independent, repeat mutations to the same nucleotide state.
249 In order to test this, we plotted the population-level mutations per day (including repeat
250 mutations at variable sites), which did not reveal any increase in mutation rate at the time of the
251 B.1.1.7 and in fact displayed a *decrease* with the emergence of the late_2020_VOC (Figure 3c,
252 Figure S1). Possible explanations are either a large increase in mutations in a small number of

253 individuals over a short time period (that would have to occur on multiple continents to explain
254 B.1.1.7, B.1.351, and P.1), or recombination between two or more divergent haplotypes carrying
255 the VOC mutations (Figure 3d).

256 Recombination is the most parsimonious explanation given (1) the absence of a
257 substantial increase in mutation rate at any time prior to the appearance of the VOC, (2) the
258 widespread and early circulation of the majority of the mutations associated with them in other
259 haplotypes and, (3) that several mutations appear disjointly across the MJN (Figure 2a). The
260 first notable disjoint mutation is $Ser^{477}Asn$ in S that defines D.2 along with nsp2 $Ile^{120}Phe$
261 (Figure 2a), which then appears in B.1.160. Likewise, $Asn^{501}Tyr$ and $Pro^{681}His$ in S appear in
262 divergent haplotypes, including one mink subgroup from Denmark and a basal node to B.1.351
263 (without the nsp6 deletion). It could be argued that those in S ($Asn^{501}Tyr$, $Ser^{477}Asn$, and
264 $Pro^{681}His$) are the result of multiple independent mutation events because they are under positive
265 selection (Martin et al. 2021), but we also identified a mutation in nsp3 that is one of the lineage-
266 defining mutations for B.1.1.7 and appears in disjoint nodes, but is unlikely to be under selection
267 because it is synonymous. It should also be noted that recombination can generate a high
268 number of false-positives when testing for signs of positive selection (Anisimova et al. 2003),
269 and the complexity of coronavirus recombinants compared to those generated in diploid
270 organisms through homologous chromosome crossovers (Figure 3d) makes that process difficult
271 to detect. Therefore, analyses that test for positive selection based on multiple independent
272 mutations at a site may, in fact, be false positives that result from recombination events. The
273 majority of the mutations found in B.1.1.7 could be explained by the admixture and
274 recombination among lineages and a random scan of 100 FASTQ files from B.1.1.7 available in
275 the NCBI SRA database identified two co-infected individuals in further support of this
276 hypothesis (Table S2). Large-scale analyses of these data may enable the detection of
277 recombinants.

278

279

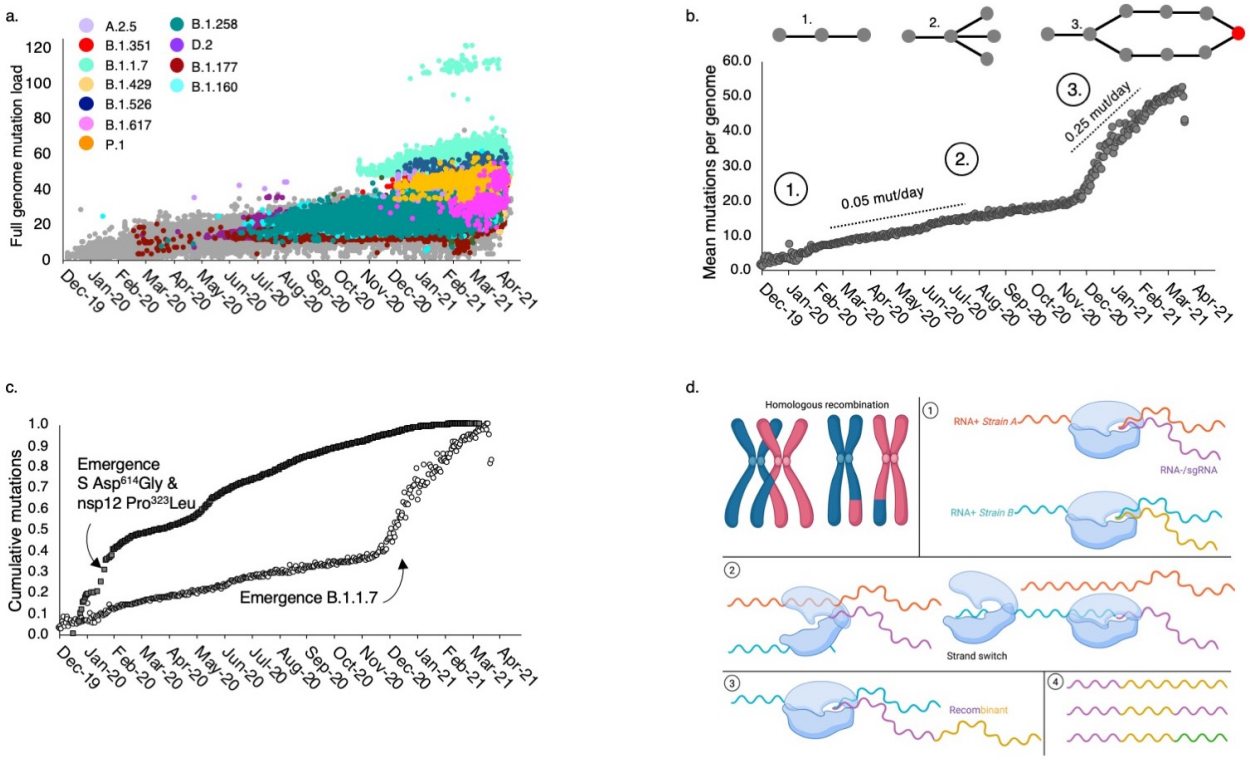

Fig. 3 Mutation rates and genomic mutation load of SARS-CoV-2. a. A rapid increase in the number of mutations per individual genome is evident in the late_2020_VOC. The outliers of the B.1.1.7 lineages (mint green) are a subset of that lineage due to a single, 57 base pair deletion in ORF7a (amino acids 5-23). **b.** Mean mutation load per individual, based on 2,128 high-confidence sites by date. The SARS-CoV-2 virus accumulated an estimated 0.05 mutations per day until the appearance of B.1.1.7, when it increased five-fold. Circles with numbers denote three processes occurring at different timepoints: (1) emergence, (2) haplotype expansion, and (3) recombination of divergent lineages. **c.** A population-level analysis of new mutations per day over the same time period (dark squares) displays a declining rate of mutations with a slight increase around the emergence of D.2 in Australia but not an increase with the emergence of B.1.1.7 that could explain the rapid accumulation of mutations shown in (b) plotted as percent accumulation (unfilled circles). **d**. Recombination in a diploid organism results from the crossover of homologous chromosomes during meiosis. In RNA+ betacoronaviruses, recombination occurs when two or more strains (haplotypes) infect a single cell (1). The replisome dissociates (2) from one strand and switches to another, (3) generating a hybrid recombinant. The resulting chimera (4) can be as simple as a section of *strain A* fused to a section of *strain B* or more complex recombinants if strand switching occurs more than once or there are multiple strains per cell (green section). Reference sequence: NC_045512, Wuhan, December 24, 2019.

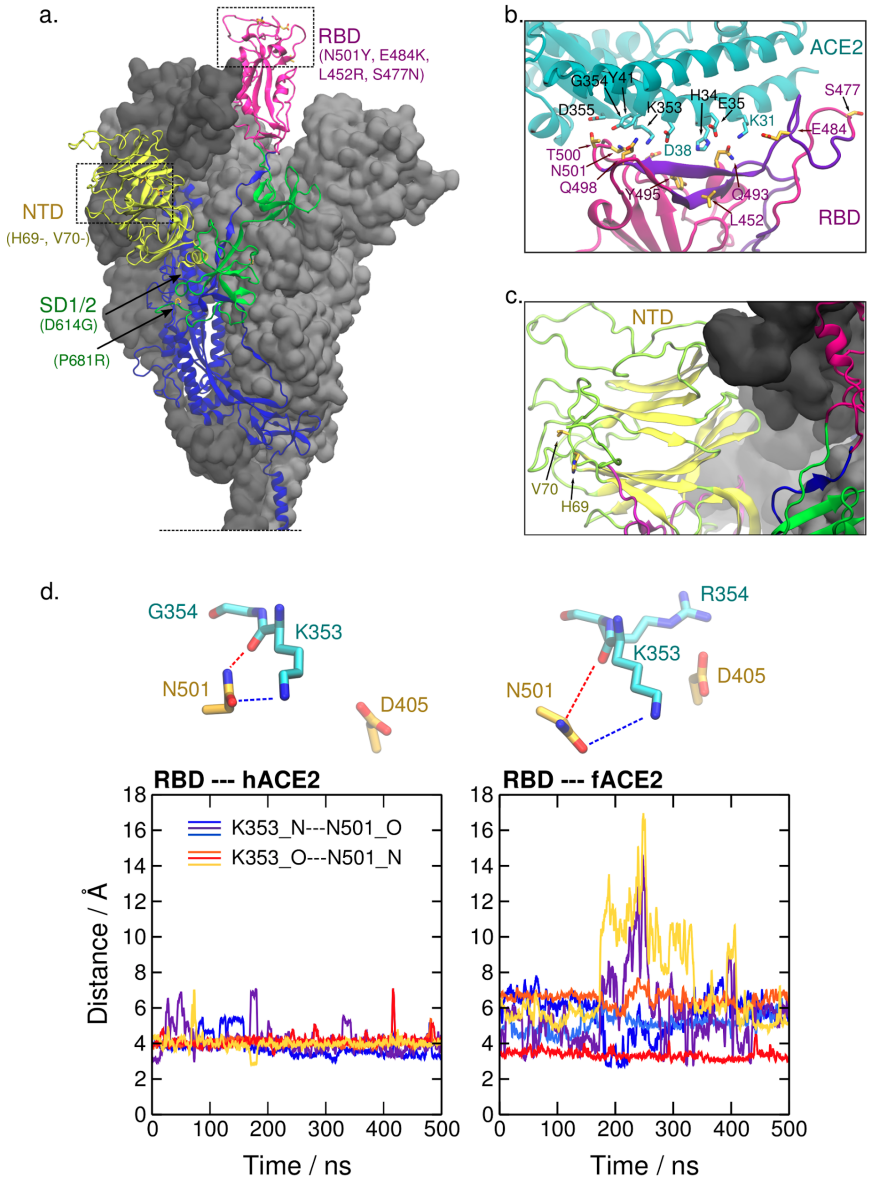

Fig. 4. Location of mutation sites of SARS-CoV-2 VOC on the structure of the spike glycoprotein. a. Several mutations associated with dominant haplotypes are located in the receptor-binding domain (RBD, aa. 331-506), N-terminal domain (NTD, aa. 13-305), and subdomains 1 and 2 (SD1/2, aa. 528-685) of S. The structure of S in the prefusion conformation derived from PDB ID 6VSB (Wrapp et al. 2020) and completed *in silico* (Casalino et al. 2020) is shown. Glycosyl chains are not depicted, and the S trimer is truncated at the connecting domain for visual clarity. The secondary structure framework of one protomer is represented and the neighboring protomers are shown as a gray surface. **b.** Mutation sites in the S RBD of SARS-CoV-2 VOC, such as 484, 452, 477, and 501 are located at or near the interface with ACE2. Notably, site 452 and 484 reside in an epitope that is a target of the adaptive immune response in humans (aa. 480-499, in violet) and site 501 is also located near it (B.-Z. Zhang et al. 2020). Dashed lines represent relevant polar interactions discussed here. PDB ID 6M17 was used (R. Yan et al. 2020). **c.** The sites 69 and 70 on the NTD, which are deleted in the VOC B.1.1.7, are also found near an epitope (aa. 21-45, in violet) (B.-Z. Zhang et al. 2020). **d.** Time progression of N---O distances between atoms of Asn^{501} in RBD and Lys^{353} in human and ferret ACE2 (hACE2 and fACE2, respectively) from the last 500 ns of the simulation runs.

Colors in the plots correspond to the distances Lys^{353}_N---Asn^{501}_O (cold colors) and Lys^{353}_O---Asn^{501}_N (warm colors) in three independent simulations of each system. These distances are represented in the upper part of the figure.

The potential functional impact of key mutations in S and non-S proteins

Given the results from the MJN analysis and our previous hypothesis (Garvin, Prates, et al. 2020) that the cooperative effects of mutations in S and non-S proteins (i.e., epistasis) define and are responsible for the increased transmission of prevalent SARS-CoV-2 variants (Lauring and Hodcroft 2021), we performed protein structural analyses and discuss below the functional effects of these individual and combined mutations in SARS-CoV-2 VOC. We analyze ten likely key mutation sites (red font, Table 1) in S and non-S proteins.

S Asn^{501}Tyr - Located in the receptor-binding domain (RBD) of SARS-CoV-2 S, immunoprecipitation assays reveal that site 501 plays a major role in the affinity of the virus to the host receptor, ACE2 (Shang et al. 2020). Via structural analysis and extensive molecular dynamics simulations, Ali et al. highlighted the importance of the interactions with human ACE2 (hACE2) near the site 501 of the receptor-binding domain of S, particularly via a sustained hydrogen bond between RBD Asn^{498} and hACE2 Lys^{353} (Ali and Vijayan 2020). Deep mutational scanning of SARS-CoV-2 RBD reveals that the naturally occurring mutations at site 501, Asn^{501}Tyr and Asn^{501}Thr, lead to an increased affinity to hACE2 (Starr et al.). Additionally, this site is located near a linear B cell immunodominant site (B.-Z. Zhang et al. 2020), and therefore the mutation may allow SARS-CoV-2 variants to escape neutralizing antibodies (Figure 4, Figure 5). Indeed, neutralizing antibodies derived from vaccinations and natural infection have significantly reduced activity against pseudotyped viruses carrying this mutation (Wang et al. 2021).

Table 2. Surface exposed residues of ACE2 orthologues forming the region of contact with site 501 of SARS-CoV-2 S. Relative to the human sequence, almost all these residues are either conserved ("|") or replaced by a nearly equivalent amino acid in mouse, American mink, European mink, ferret, and pangolin. Notably, there is a nonconservative substitution of Gly^{354} to a bulky positively charged amino acid in most species. Our structural analyses suggests that this substitution contributes to a putative host-dependent selective pressure at site 501 of SARS-CoV-2 S. Prevalent residues reported at this site are informed in order of frequency.

Species	Residues in ACE2									S 501
***Homo sapiens* (Human)**	**D38**	**Y41**	**Q42**	**L45**	**K353**	**G354**	**D355**	**R357**	**I358**	**Y, N**
Mus musculus (House mouse)	I	I	I	I	H	I	I	I	I	Y, N
Neovison vison (American mink)	E	I	I	I	I	H	I	I	I	N, T
Mustela lutreola (European mink)	E	I	I	I	I	R	I	I	I	N, T
Mustela putorius furo (Ferret)	E	I	I	I	I	R	I	I	I	T, N
Manis pentadactyla (Pangolin)	E	I	I	I	I	H	I	I	I	N, T

342

343 Transmission between human and non-human hosts for SARS-CoV-2 provides further
344 information on the evolutionary selectivity of site 501 in S. Repeated infection of mice with
345 human SARS-CoV-2 resulted in the selection of a mouse-adapted strain carrying S Tyr^{501} (Gu et
346 al. 2020). It is possible that Asn^{501}Tyr results in an additional stabilization of the RBD-ACE2
347 interaction via π-stacking of Tyr^{501} with Tyr^{41} in ACE2 (Figure 4a-b). In contrast, several
348 introductions into farmed mink (*Neovison vison*), which caused a substantial increase in their
349 mortality (Oude Munnink et al. 2021), have not led to the same selection. To date, reported
350 sequences in GISAID of SARS-CoV-2 in this host carry either S Asn^{501}, which is prevalent, or S
351 Thr^{501}, which appeared independently in mink farms (Table S3) (Oude Munnink et al. 2021). In
352 ACE2 of these taxa, Tyr^{41} is conserved, but near this site, a larger, positively charged amino
353 acid, His^{354}, replaces Gly^{354}. Table 2 shows that the amino acids in the RBD 501-binding region
354 of the ACE2 orthologues are conserved, except for Gly^{354}, indicating that this site may play a key
355 role in viral fitness.

356

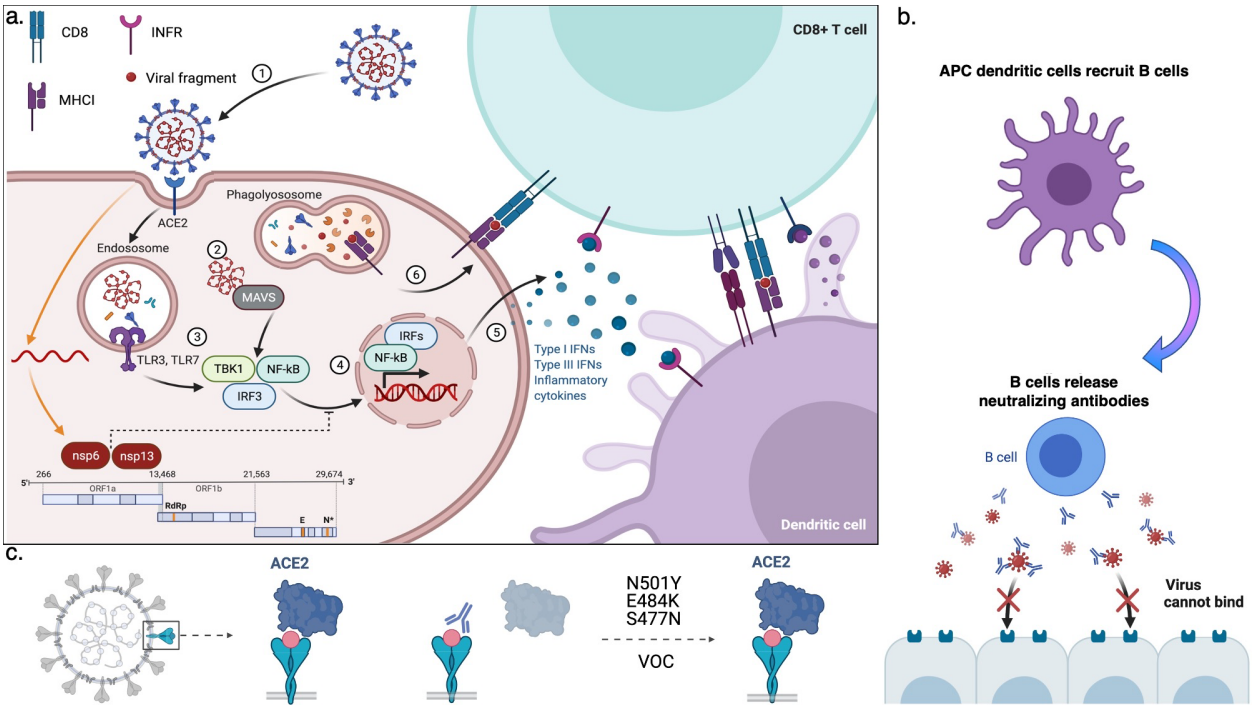

Fig. 5. Response to viral infection. a. As part of the innate immune response, (Step 1) the SARS-CoV-2 virus is internalized into endosomes and degraded. (Step 2) viral RNA activates the mitochondrial antiviral innate immunity (MAVS) pathway and (Step 3) degraded proteins activate the toll receptor pathway (TLR3/TLR7), which result in the (Step 4) phosphorylation of TBK1 and translocation of NF-*k*B and IRF3 to the nucleus, where they regulate the transcription of immune genes including interferons (IFNs, Step 5). IFNs recruit CD8+ T cells that, (Step 6) recognize fragments of the virus on the cell surface via their class I major histocompatibility complex (MHC I) receptors and are activated by dendritic cells (antigen processing cells, or APC). If the virus bypasses innate immunity (orange arrows) nonstructural proteins (nsp6 and nsp13) block the IRF3 nuclear translocation. **b.** APCs recruit B lymphocytes and stimulate the production of antibodies that recognize SARS-CoV-2 S (whereas T cells recognize fragments of S bound to MHC I). **c.** The neutralizing antibodies block binding of the virus to the ACE2 receptor and can prevent re-infection but mutations in the receptor-binding domain (RBD), e.g., S Asn^{501}Tyr, prevent binding of the antibodies and the virus is then able to bind the receptor again even if individuals experienced exposure to an earlier strain or were vaccinated. *Created with BioRender.com.*

Similarly, ferrets (*Mustela putorius furo*) and pangolins (*Manis pentadactyla)*, relevant potential reservoirs of SARS-CoV-2, carry a large basic residue at site 354 (an arginine and histidine, respectively). Sawatzki et al. reported that the constant exposure of ferrets to infected humans did not result in natural transmission in a domestic setting, suggesting that ferret infection may require improved viral fitness (Sawatzki et al. 2021). In agreement with that, Richard et al. (Richard et al. 2020) reported that the adaptive substitution Asn^{501}Thr was detected in all experimentally infected ferrets in the laboratory. In order to further investigate the role of the Gly^{354} versus Arg^{354} in the adaptive mutation of site 501 in S RBD, we performed extensive

380 molecular dynamics simulations of the truncated complexes of Asn^{501}-carrying RBD of SARS-
381 CoV-2 and ACE2, from human (hACE2) and ferret (fACE2). The simulations indicate that there
382 is a remarkable difference in the interaction pattern between the two systems in the region
383 surrounding site 501 of RBD. Firstly, we identified the main ACE2 contacts with Asn^{501}, which
384 were the same for both species, namely, Tyr^{41}, Lys^{353}, and Asp^{355}, and we also show that the
385 intensity of these contacts is lower in the simulations of fACE2 (Table S4).

386 To investigate further, we analyzed structural features in the interaction between ACE2
387 Lys^{353} and RBD Asn^{501}. Distances between polar atoms computed from the simulations indicate
388 a weaker electrostatic interaction between this pair of residues in ferret compared to human
389 (Figure 4d). This effect is accompanied by a conformational change of fACE2 Lys^{353}. Figure S2
390 shows that, in ferret, the side chain of Lys^{353} exhibits more stretched conformations, i.e., a higher
391 population of the *trans* mode of the dihedral angle formed by the side chain carbon atoms. This
392 conformational difference could be partially attributed to the electrostatic repulsion between the
393 two consecutive bulky positively charged amino acids in ferrets, Lys^{353} and Arg^{354}. Additionally,
394 the simulations suggest a correlation, in a competitive manner, between other interactions that
395 these residues display with the RBD. For example, Figure S3 shows that the salt bridge
396 fACE2_Arg^{354}---RBD_Asp^{405} and the HB interaction fACE2_Lys^{353}---RBD_Tyr^{495} (backbone)
397 alternate in the simulations. This also suggests that the salt bridge formed by fACE2 Arg^{354} drags
398 Lys^{353} apart from RBD Asn^{501}, weakening the interaction between this pair of residues in ferrets
399 relative to humans.

400 Altogether, these analyses indicate that site 354 in ACE2 significantly influences the
401 interactions with RBD in the region of site 501 and is likely playing a major role in the
402 selectivity of the size and chemical properties of this residue in SARS-CoV-2. We propose that,
403 in contrast to Tyr^{501}, a smaller HB-interacting amino acid at site 501 of RBD, such as the
404 threonine reported in farmed mink and ferrets, may ease the interactions on the region, e.g., the
405 salt bridge between fACE2 Arg^{354} and RBD Asp^{405}. The differences in the region of ACE2 in
406 contact with site 501 seem to have a key role for host adaptation and are worth further
407 investigation as it may also reveal details of the origin of this zoonotic pandemic.

408 *S His^{69}_Val^{70} deletion* - The His^{69}_Val^{70} deletion (in B.1.1.7) is adjacent to a linear epitope at the

409 N-terminal domain of S (Figure 4a,c) (B.-Z. Zhang et al. 2020), suggesting it too may improve
410 fitness by reducing host antibody effectiveness.

411 *S Leu^{452}Arg* - The Leu^{452}Arg mutation in S is a core change in the early_2021_VOC (Table 1,
412 Figure 4a-b). Although Leu^{452} does not interact directly with ACE2, this mutation was shown to
413 moderately increase infectivity in cell cultures and lung organoids using Leu^{452}Arg-carrying
414 pseudovirus (Deng et al. 2021). It is possible that the substitution of the leucine, hydrophobic, to
415 arginine, a positively charged residue, creates a direct binding site with ACE2 via the
416 electrostatic interaction with Glu^{35}. However, in Starr et al., experiments with the isolated RBD
417 expressed on the cell surface of yeast show that this mutation is associated with enhanced
418 structural stability of RBD, while it only slightly improves ACE2-binding (Starr et al.). An
419 alternative but not mutually exclusive hypothesis is that it causes a local conformational change
420 that impacts the complex dynamic interchange between interactions of RBD with the spike
421 trimer itself and with the host receptor. Noteworthy, site 452 resides in a significant
422 conformational epitope in RBD and Leu^{452}Arg was shown to decrease binding to neutralizing
423 antibodies (Figure 4b) (Deng et al. 2021; Li et al. 2021).

424 As noted in Deng et al., S Leu^{425}Arg has been reported in rare variants starting in March 2020
425 from Denmark, i.e., several months before the surge of the VOC that carry this mutation
426 (B.1.427, B.1.429, and B.1.617) (Deng et al. 2021). This indicates that the high transmissibility
427 of the early_2021_VOC is not fully explained by the increased infectivity caused by Leu^{425}Arg
428 and combined mutations may be essential for the rapid spread. Besides the other mutations in the
429 spike in these VOC, the substitution Asp^{260}Tyr in the SARS-CoV-2 helicase (nsp13, below) is
430 especially interesting, as it was identified in the MJN analysis as a defining mutation of both
431 B.1.427 and B.1.429 variants.

432 *S Ser^{477}Asn* - Variants carrying the S Ser^{477}Asn mutation spread rapidly in Australia (Figure 1,
433 Figure 3b). This site, located at the loop β4-5 of the RBD, is predicted not to establish persistent
434 interactions with ACE2 (Ali and Vijayan 2020). However, deep scanning shows that this
435 mutation is associated with a slight enhancement of ACE2-binding. Molecular dynamics
436 simulations suggest that Ser^{477}Asn affects the local flexibility of the RBD at the ACE2-binding
437 interface, which could be underlying the highest binding affinity with ACE2 reported from

438 potential mean force calculations (Singh et al.). Additionally, this site is located near an epitope
439 and may alter antibody recognition and counteract the host immune response (Figure 4b).

440 *S Glu^{484}Lys* - A recent computational study suggests that Glu^{484} exhibits only intermittent
441 interactions with Lys^{31} in ACE2 (Ali and Vijayan 2020). Deep scanning shows that this mutation
442 is associated with higher affinity to ACE2 (Starr et al.) and may be explained by its proximity to
443 Glu^{75} in ACE2, which would form a salt bridge with Lys^{484}. Aside from the potential impact of
444 Glu^{484}Lys between virus-host cell interaction, this site is part of a linear B cell immunodominant
445 site (B.-Z. Zhang et al. 2020) and this mutation was shown to impair antibody neutralization
446 (Wang et al. 2021).

447 *S Pro^{681}Arg and Pro^{681}His* - These mutations in the multibasic furin cleavage site are particularly
448 relevant given the importance of this region for cell-cell fusion (Hoffmann et al. 2020; Papa et
449 al.). The presence of the multibasic motif of SARS-CoV-2 has shown to be essential to the
450 formation of syncytia (i.e., multinucleate fused cells), and thus it is thought to be a key factor
451 underlying pathogenicity and virulence differences between SARS-CoV-2 and other related
452 betacoronaviruses. Hoffmann et al. recognized the importance of the furin cleavage site in
453 SARS-CoV-2 and its biochemically basic signature and generated mutants to determine the
454 effects of specific amino acids. Notably, they showed that pseudotyped virion particles bearing
455 mutant SARS-CoV-2 S with additional basic residues in this region, including the substitution
456 Pro^{681}Arg (present in B.1.617), exhibits a remarkable increase in syncytium formation in lung
457 cells *in vitro* (Hoffmann et al. 2020), which may explain the increased severity of the disease
458 (Sheikh et al. 2021). Hoffman et al did not include a Pro^{681}His change that is a defining mutation
459 of B.1.1.7, and so it is not known if this too increases syncytium formation given that it is a basic
460 amino acid, but should be the target of future studies.

461 *Nucleocapsid Arg^{203}Met* - The main function of the nucleocapsid (N) protein in SARS-CoV-2 is
462 to act as a scaffold for the viral genome and it is also the most antigenic protein produced by the
463 virus (Dutta et al. 2020). In a previous study, we reported that the Ser-Arg-rich motif of this
464 protein (a.a. 183-206), shown *in vitro* to be necessary for viral replication (Tylor et al. 2009;
465 Garvin, Prates, et al. 2020), displays a high number of amino acid changes during the COVID-
466 19 pandemic and is likely under positive selection. We propose that the RNA gene segment

467 coding this particular subsequence may be linked to improved fitness of specific SARS-CoV-2
468 haplotypes including the rapidly spreading Delta variant and is linked to epigenetic alterations
469 (Figure 6a).

470 A recent deep transcriptome sequencing study used Oxford Nanopore^{TM} technology to
471 detect epigenetic modifications at 41 sites in the RNA genome that are associated with leader
472 sequence addition to sub-genomic RNA transcripts, a recombination-like process of SARS-CoV-
473 2 (Kim et al. 2020). Nanopore instruments can detect epigenetic modifications based on
474 disruptions of the electrical current as the RNA molecule passes through the molecular pore
475 (Rand et al. 2017; Simpson et al. 2017), which Kim et al propose is responsible for the pause that
476 occurs before leader sequence addition. Twenty-five of the 41 modified sites reside in the N gene
477 and the majority of the sites in this subset are found near the Ser-Arg-rich motif (Figure 6a).

478 Furthermore, one specific epigenetic site is linked to two highly successful SARS-CoV-2
479 haplotypes. The first is a triple mutation at sites 28881-28883 (GGG to AAC, $Arg^{203}Lys$) that is
480 now found in nearly half of all sequences sampled across the globe (diamond nodes, Figure 1)
481 and the second is $Arg^{203}Met$, which is a defining mutation for the rapidly spreading B.1.617.
482 Notably, this region of the genome is highly conserved across several hundred years of
483 coronavirus evolution (Boni et al. 2020) (Figure 6a). Given that these epigenetic sites were
484 discovered because the RNA pauses as it passes across the pore of the molecular nanopore
485 sequencer, one interesting hypothesis is that mutations at this region remove the epigenetic
486 modification and speed the SARS-CoV-2 genome through the replisome (Figure 6b), increasing
487 the production of virions, which is consistent with the more than 1000-fold higher virion count in
488 those infected with B.1.617 (Lu et al.).

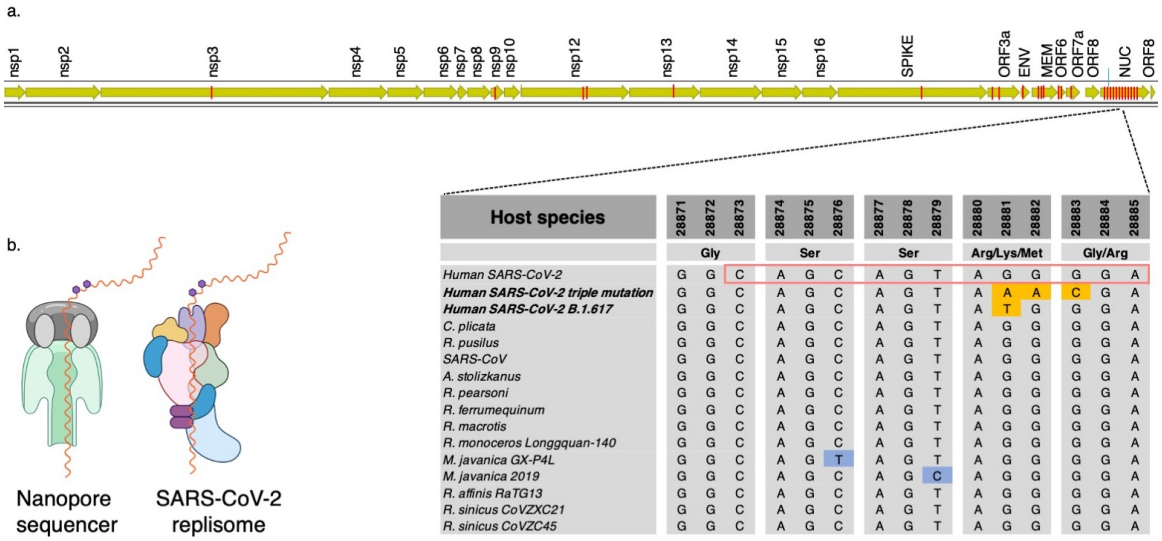

Host species	28871	28872	28873	28874	28875	28876	28877	28878	28879	28880	28881	28882	28883	28884	28885
	Gly			Ser			Ser			Arg/Lys/Met			Gly/Arg		
Human SARS-CoV-2	G	G	C	A	G	C	A	G	T	A	G	G	G	G	A
Human SARS-CoV-2 triple mutation	G	G	C	A	G	C	A	G	T	A	A	A	C	G	A
Human SARS-CoV-2 B.1.617	G	G	C	A	G	C	A	G	T	A	T	G	G	G	A
C. plicata	G	G	C	A	G	C	A	G	T	A	G	G	G	G	A
R. pusilus	G	G	C	A	G	C	A	G	T	A	G	G	G	G	A
SARS-CoV	G	G	C	A	G	C	A	G	T	A	G	G	G	G	A
A. stolizkanus	G	G	C	A	G	C	A	G	T	A	G	G	G	G	A
R. pearsoni	G	G	C	A	G	C	A	G	T	A	G	G	G	G	A
R. ferrumequinum	G	G	C	A	G	C	A	G	T	A	G	G	G	G	A
R. macrotis	G	G	C	A	G	C	A	G	T	A	G	G	G	G	A
R. monoceros Longgquan-140	G	G	C	A	G	C	A	G	T	A	G	G	G	G	A
M. javanica GX-P4L	G	G	C	A	G	T	A	G	T	A	G	G	G	G	A
M. javanica 2019	G	G	C	A	G	C	A	G	C	A	G	G	G	G	A
R. affinis RaTG13	G	G	C	A	G	C	A	G	T	A	G	G	G	G	A
R. sinicus CoVZXC21	G	G	C	A	G	C	A	G	T	A	G	G	G	G	A
R. sinicus CoVZC45	G	G	C	A	G	C	A	G	T	A	G	G	G	G	A

Fig. 6. Modifications at the Ser-Arg-rich region of N may affect replication speed. a. Location of 41 epigenetic sites reported in Kim et al. 2020 (red bars on SARS-CoV-2 genome). One of the sites in the nucleocapsid gene (nucleotides in red box of aligned sequences) is highly conserved across diverse host-defined coronaviruses. All bats and human coronavirus species from China are completely conserved at the epigenetic site 28881-28883, except for a 3-bp mutation in SARS-CoV-2 that occurred early in the pandemic and now corresponds to ~50% of all sequences globally (diamond nodes in Figure 1). **b.** Kim et al. proposed that N^6-methyladeonsine modification of the genome (purple hexagons), common in RNA viruses, caused the strand to pause while traversing the nanopore sequencing apparatus. We propose that loss of this site via mutations at site 203 in N may increase the replication rate of the RNA strand through the SARS-CoV-2 replisome. *Aselliscus stoliczkanus* - Stoliczka's trident bat, *Chaerephon plicata* - wrinkle-lipped free-tailed bat, *Rhinolophus pusillus* - least horseshoe bat, *R. pearsoni* - Pearson's horseshoe bat, *R. macrotis* - big-eared horseshoe bat, *R. ferrumequinum* - greater horseshoe bat, *R. monoceros* - Formosan lesser horseshoe bat, *R. affinis* intermediate horseshoe bat, *R. sinicus* Chinese rufous horseshoe bat, *R. mayalanis* - Mayalan horseshoe bat, *SARS* - Severe Acute Respiratory Syndrome, *Manis javanica* - Malayan pangolin. *Created with BioRender.com.*

nsp2 Ile^{120}Phe - The main role of the nonstructural protein 2 (nsp2) in viral performance is not yet defined. Instead, this protein appears to be part of multiple interactions with host proteins involved in a range of processes including the regulation of mitochondrial respiratory function, endosomal transport, and ribosome biogenesis (Verba et al. 2021). Very recently, deep learning-based methods of structure prediction and cryo-electron microscopy density were combined to provide the atomic model of nsp2 (PDB id 7MSW). In a preprint from Verba et al., structural information was used to localize the surfaces that are key for protein-protein interaction with nsp2 (Verba et al. 2021). From structural analysis and mass spectrometry experiments, the

514 authors pose the interesting hypothesis that nsp2 interacts directly with ribosomal RNA via a
515 highly conserved zinc ribbon motif to bring ribosomes close to the replication-transcription
516 complexes.

517 Here we are particularly interested in the functional impact of the mutation $Ile^{120}Phe$ in nsp2
518 present in the D.2 variant. Site 120, identified in the nsp2 structure on Figure 7a, is a point of
519 hydrophobic contact between a small helix, rich in positively charged residues, and a zinc
520 binding site. The positively charged surface of the helix may be especially relevant for a putative
521 interaction with the phosphate groups from ribosomal RNA. Normal mode analysis from
522 DynaMut2 predicts that the substitution has a destabilizing effect in the protein structure
523 (estimated $\Delta\Delta G^{stability}$ = -2 kcal/mol) (Rodrigues et al. 2021). Possibly, this could be caused by π-
524 π stacking interactions of the tyrosine with aromatic residues in the same helix that would disrupt
525 the contacts anchoring it to the protein core (Figure 7b). Additionally, site 120 is spatially close
526 to Glu^{63} and Glu^{66}, which were shown to be relevant for interactions with the endosomal/actin
527 machinery via affinity purification mass spectrometry in HEK293T cells. Remarkably, upon
528 mutation of these glutamates to lysines, there is increased interactions with proteins involved in
529 ribosome biogenesis (Verba et al. 2021).

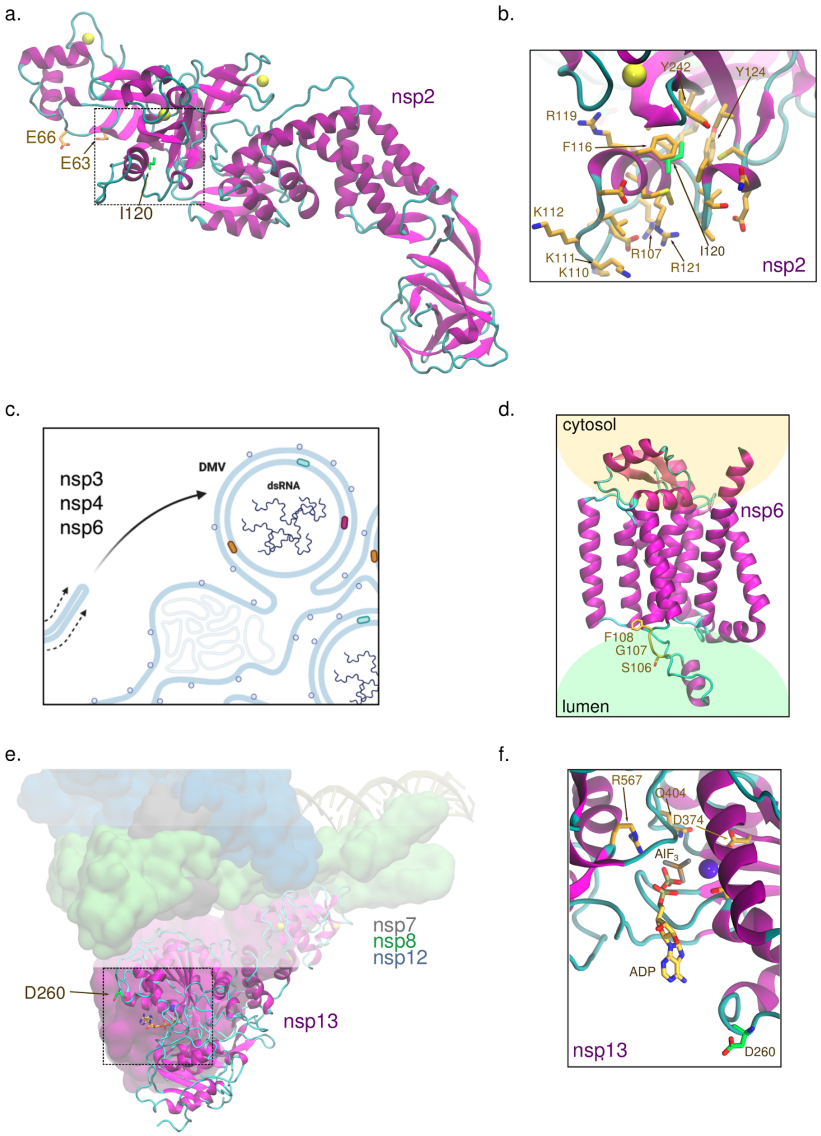

530

531 **Fig. 7. Location of mutations of prevalent SARS-CoV-2 variants on the structure of the nonstructural**
532 **proteins nsp2, nsp6, and nsp13. a.** Site 120 in nsp2 is located in a small helix near a zinc-binding site and residues
533 Glu^{63} and Glu^{66}, which play a role in the interaction with proteins involved in ribosome biogenesis and in the
534 endosomal/actin machinery (Verba et al. 2021). PDB id 7MSW was used. **b.** Ile^{120} forms some of the hydrophobic
535 contacts that anchor the helix at the surface of nsp2, where this site resides, to the protein core. **c.** Nsp6 participates
536 in generating double-membrane vesicles (DMV) for viral genome replication. Natural selection for the biological
537 traits of viral entry and replication may explain the increased transmission of variants with adaptive mutations in
538 both S and nsp6. DMVs isolate the viral genome from host cell attack to provide for efficient genome and sub-
539 genome replication and generate virions. **d.** Sites 106-108 are predicted to be located at/near the protein region of
540 nsp6 embedded in the endoplasmic reticulum lumen (structure generated by AlphaFold2 (Jumper et al.)). **e.** Nsp13 is
541 the SARS-CoV-2 helicase, and it is part of the replication complex. **f.** Asp^{260} in nsp13 is mutated to tyrosine in
542 B.1.427 and B.1.429 and it is located at the entrance of the NTP-binding site. PDB id 6XEZ was used (Chen et al.
543 2020).

544 *nsp6 Ser^{106}_Phe^{108}deletion* - The nsp6 protein plays critical roles in viral replication and
545 suppression of the host immune response (Figure 5a and Figure 7c) (Gupta et al. 2020). Along

546 with nsp3 and nsp4, nsp6 is responsible for producing double-membrane vesicles from the
547 endoplasmic reticulum (ER) to protect the viral RNA from host attack and increase replication
548 efficiency (Figure 7c) (Santerre et al. 2020). The nsp6 Ser^{106}_Phe^{108}del is predicted to be located
549 at a loop in the interface between a transmembrane helix and the ER lumen based on a
550 preliminary structural analysis of the model generated by the AlphaFold2 system (Figure 7d),
551 and we hypothesize that the deletion may affect functional interactions of nsp6 with other
552 proteins. In addition, in agreement with the enhanced suppression of innate immune response
553 reported for B.1.1.7 (Thorne et al. 2021), changes in immune-antagonists, such as nsp6
554 Ser^{106}_Phe^{108}del, may be key to prolonged viral shedding (Calistri et al. 2021).

555 *nsp13 Asp^{260}Tyr* - The nonstructural protein 13 is a component of the viral replication-
556 transcription complex, (nsp13; or SARS-CoV-2 helicase) and plays an essential role in
557 unwinding the duplex oligonucleotides into single strands in a NTP-dependent manner (L. Yan et
558 al. 2020). Hydrogen/deuterium exchange mass spectrometry demonstrates that the helicase and
559 NTPase activities of SARS-CoV nsp13 are highly coordinated, and mutations at the NTPase
560 active site impair both ATP hydrolysis and the unwinding process (Jia et al. 2019). Here we note
561 that the substitution Asp^{260}Tyr, present in B.1.427 and B.1.429, is located at the entrance of the
562 NTPase active site and may favor π-π stacking interactions with nucleobases (Figure 7e-f). Given
563 that, at high ATP concentrations, SARS-CoV nsp13 exhibits increased helicase activity on
564 duplex RNA (Jang et al. 2020), it is possible that, similarly, the putative optimization on NPT
565 uptake in nsp13 Asp^{260}Tyr favors RNA unwinding.

566 Additionally, nsp13 was shown to play an important role as an innate immune antagonist
567 (Figure 5a). It contributes to the inhibition of the type I interferon response by directly binding to
568 TBK1 and, with that, it impedes IRF3 phosphorylation (Guo et al. 2021). The dual role of nsp6
569 and nsp13 in immune suppression and viral replication may suggest a convergent evolution of
570 SARS-CoV-2 manifested in most of the VOC, which carries either nsp6 Ser^{106}_Phe^{108}del or
571 nsp13 Asp^{260}Tyr.

572

573 **3. Concluding Remarks**

574 From our thorough analysis of the spatiotemporal relationships of SARS-CoV-2 variants, we
575 propose that the rapid increase of mutations in the late 2020 VOC is likely a consequence of the
576 recombination of haplotypes carrying adaptive mutations in S and in non-S proteins that act
577 cooperatively to enhance viral fitness. For example, as indicative of that, we call attention to five
578 mutations that occur independently in disjoint clusters of our MJN, four of which (S Asn^{501}Tyr,
579 S His^{69}_Val^{70}del, S Phe^{681}His/Arg, and nsp6 Ser^{106}_Phe^{108}del) are shared by different VOC,
580 including B.1.1.7. Notably, S His^{69}_Val^{70}del appeared in human and mink populations
581 simultaneously in August 2020, prior to the emergence of B.1.1.7, indicating that mink should be
582 further investigated as a possible component of a recombination event. In turn, our molecular
583 dynamics simulations indicate that the molecular forces at site 501 in S and how they are altered
584 upon mutation (S Asn^{501}Tyr in B.1.1.7) are a key component to describe the history of
585 transmission among other putative zoonotic reservoirs, such as farmed minks, ferrets, and
586 pangolins.

587 The S Asp^{614}Gly mutation has been shown to increase infectivity and is now predominant
588 in the circulating virus (L. Zhang et al. 2020), and S Asn^{501}Tyr is associated with higher
589 virulence (Gu et al. 2020). We show that the expansion of the strains carrying these mutations
590 only occurred upon the additional substitutions in nsp12 Leu^{323}Pro (Figure 2b) (Garvin, Prates, et
591 al. 2020) and nsp6 Ser^{106}_Phe^{108}del, respectively. A hypothesis consistent with these
592 observations is that the changes in S enhance viral entry into the host cells but they do not easily
593 transmit due to rapid suppression by a robust innate immune response. A secondary mutation is
594 able to counteract the immune-driven suppression. In the case of S Asp^{614}Gly, the nsp12
595 Leu^{323}Pro may have increased the replication rate of the virus, which was supported by
596 quantitative PCR from clinical samples with different viral strains in Korber et al. (Garvin,
597 Prates, et al. 2020; Korber et al. 2020). However, the separate effects of S Asp^{614}Gly and nsp12
598 Leu^{323}Pro could not be described in the referred study because it did not include individuals
599 infected with variants harboring only one of the mutations.

600 For the late 2020 VOC, nsp6 Ser^{106}_Phe^{108}del may affect viral replication in DMVs or
601 suppress the interferon-driven antiviral response (Xia et al. 2020). It is likely that other mutations
602 also enhance viral mechanisms that impair the host immune response. For example, Thorne et al.
603 recently showed that the B.1.1.7 VOC suppresses the innate immune response by host cells *in*

604 *vitro* and attributed it to the increased transcription of the *orf9b* gene, nested within the gene
605 coding the nucleocapsid protein. (Thorne et al. 2021), although they could not rule out the
606 possibility that this was due to nsp6 Ser^{106}_Phe^{108}del.

607 Via focused protein structural analysis, we identify other mutations shared among
608 different VOC that reside in key locations of proteins involved in viral replication and/or in
609 suppressing the innate immune suppression, such as nsp13, suggesting a convergent evolution of
610 SARS-CoV-2. This emphasizes the importance of tracking mutations in a genome-wide manner
611 as a strategy to avoid the emergence of future VOC. For example, an earlier dominant variant in
612 Australia (D.2) that carried the mutations Ser^{477}Asn in S and Ile^{120}Phe in nsp6 was successfully
613 restrained. However, we note that variants harboring only the S Ser^{477}Asn substitution are
614 currently circulating in several European countries (Figure 2, Table S5) and may only need to
615 recombine with a variant carrying an advantageous complementary mutation to become the next
616 VOC.

617 A second and equally significant outcome from recombination-driven haplotypes is the
618 generation of variants that allow escape from neutralizing antibodies produced by an adaptive
619 immune response (Garvin, T Prates, et al. 2020) (Figure 5c). As a case in point, the resurgence of
620 COVID-19 in Manaus, Brazil, in January 2021, where seroprevalence was above 75% in October
621 2020, is due to immune escape of new SARS-CoV-2 lineages (Sabino et al. 2021). Broad disease
622 prevalence and community spread of COVID-19 increase the probability that divergent
623 haplotypes may come in contact, thereby dramatically accelerating the evolution and
624 transmission of the virus. This emphasizes that regions with low sequence surveillance can be
625 viral breeding grounds for the next SARS-CoV-2 VOC.

626

627 **4. Methods**

628 *Sequence data pre-processing*

629 We downloaded SARS-CoV-2 sequences in FASTA format and corresponding metadata from
630 GISAID and processed as we have reported previously (Garvin, Prates, et al. 2020; Prates et al.
631 2021). To ensure that deletions were accounted for, full genome sequences were aligned with

632 MAFFT (Katoh et al. 2002) to the established reference genome (accession NC_045512),
633 uploaded into CLC Genomics Workbench, and trimmed to the start and stop codons (nsp1 start
634 site and ORF10 stop codon). Aligned sequences in tab-delimited format were imported into R to
635 count the number of variable accessions at each of the 29,409 sites.

636 Variable sites were determined with all sequences downloaded up through the end of
637 January, 2021. In order to reduce false-positive mutation sites (those that were due to technical
638 error), we selected sites that were variable in 25 or more individuals (0.01%) compared to the
639 reference (all 25 were required to be the same state: A, G, T, C, or -). We further pruned these
640 by removing sites in which 20% or more of the accessions harbored an unknown character state
641 ("N"), leaving 2,128 variable sites for downstream analyses. After removing sequences with an
642 "N" at any of these sites, we retained 280,409 individuals. Prior to submission, we updated the
643 number of sequences through April 19, 2021, keeping the same 2128 variable sites, which
644 allowed us to capture the most up-to date metadata and produced 640,211 for analysis. We kept
645 haplotypes that occurred in more than 35 individuals to remove rare or artifact-derived
646 haplotypes. For the comparison of median-joining networks and phylogenetic trees, we used
647 sequences from the pandemic sampled through the end of April 2020. We used variable sites
648 found in more than ten individuals and haplotypes found in five or more individuals as we had in
649 previous work (Garvin, Prates, et al. 2020). This produced 410 unique haplotypes based on 467
650 variable sites.

651 *Median-joining network (MJN)*

652 Haplotypes were coded in NEXUS format and uploaded to PopArt (Leigh and Bryant 2015). An
653 MJN was produced with the epsilon parameter set to 0. The networks were exported as a table
654 and visualized in Cytoscape (Shannon et al. 2003) with corresponding metadata. The date of
655 emergence of each haplotype was defined by the sample date subtracted from the report date for
656 the Wuhan reference sequence (December 24, 2019) and then one day was added to remove
657 zeros. For samples that only reported the month but no day, we recorded the day as the 15th of
658 that month. We excluded samples with no sampling date.

659 *Phylogenetic tree*

660 We used the program MrBayes to generate a phylogenetic tree (Ronquist and Huelsenbeck
661 2003). Parameters were set to *Nucmodel=4by4*, *Nst=6*, *Code=Universal*, and *Rates=Invgamma*.
662 We performed 5,000,000 mcmc generations, which produced a stable standard deviation of split
663 frequencies of 0.014. A consensus tree was generated using the 50% majority rule and visualized
664 using FigTree v1.4.4 (http://tree.bio.ed.ac.uk/software/figtree/)

665 *Estimation of genome mutation load*

666 We estimated the mutation load using two data sets. First, we used the 640,211 sequences based
667 on 2,128 variable sites used for the MJN because these represent high-confidence mutations. For
668 each of the 640,211 accessions, we counted the number of differences of the 2,128 variable sites
669 compared to the reference genome (accession NC_045512) and recorded the day of emergence.
670 The mutational load for all accessions for a given day was then averaged and this was plotted
671 across time. For the second estimate of mutation rate, we used all variable sites across the full
672 genome (29,409 sites) to include rare variants and removed all sequences with at least one
673 ambiguous site, leaving 584,119 accessions.

674 For the population-level estimate of mutation accumulation, we applied the filters used to
675 identify the 2,128 variable sites that were used for the MJN for all sequences up through April
676 19, 2021. We did not include new mutations because the B.1.1.7 VOC and its downstream
677 haplotypes had become the predominant variants globally at that time and, consequently, much
678 early information of the molecular evolution is lost when applying frequency filters on the entire
679 GISAID database. This is exacerbated with the MJN approach because the software algorithm
680 used to generate the network is computationally intractable with greater than 1,000 haplotypes
681 and therefore future efforts will either need to ignore early molecular events or use new methods
682 that can handle the large datasets and any recombination events that occur (an alternative
683 approach would be to now use the Alpha or Delta variant as the reference sequence because they
684 are now the predominant strains globally).

685 For calculations of population-level mutation accumulation, it is possible (and necessary)
686 to include all sequences to determine if mutation or recombination are the cause of the high
687 mutation load seen in the late 2020 VOC. After applying the frequency and haplotype filters, we
688 retained 5,011 variable sites that define 12,282 unique haplotypes for further analysis. Mutations

689 to five possible states (A, G, T, C, and -) were counted at each site on the first date that they
690 appeared and their appearance at later dates were excluded. Multiple mutations at a site to
691 different states were counted with this method.

692 For lineage-specific mutation curves, we extracted all sequences based on their PANGO
693 lineage listed in the metadata from GISAID that also had a sample data and plotted the
694 cumulative number over time, where time is represented by days from first appearance. To
695 estimate the rate of accumulation, we calculated the slope for the linear portion of each of the
696 curves.

697 *Probability of mutation accumulation*

698 To calculate the chance of accumulating several mutations in a certain period, the probability
699 density function for a normal distribution is used:

700 $$PDF(x) = exp(-(x-\mu)^2/2\sigma^2)/sqrt(2\,\pi * \sigma^2),$$

701 where μ is the expected number of mutations for that date, x is the measured value, and σ is the
702 standard deviation of error calculated from the data shown in Fig. 1b, considering the difference
703 between the actual and predicted number of mutations. The expected value of mutations μ for a
704 given time period is computed from the estimated rate of mutations per day (Figure 3, 0.05). c.
705 The period of interest to our discussion (June-October 2020) corresponds to 122 days, for which,
706 the integral of PDF(x=13) gives the probability of $1*10^{-15}$ to accumulate 13 mutational events.

707

708 *Screen for coinfected individuals with UK B.1.1.7*

709 We extracted 25 samples from the Sequence Read Archive at NCBI for each of the months of
710 October, November, December, and January listed as variant B.1.1.7 from the UK (Table S2) for
711 a total of 100 samples to check for coinfection. The reads were mapped to the NC_045512
712 Wuhan reference using CLC Genomics Workbench using the default parameters except for
713 length fraction and similarity fraction were set to 0.9. Three sites specific to UK B.1.1.7 were
714 analyzed for possible heterozygosity. Of the 100 we sampled, two appeared to be cases of

715 coinfection. This supports the hypothesis that the large expansion in overall mutations seen in
716 UK B.1.1.7 are likely due to recombination. In addition, it also supports the case that coinfection
717 is occurring at a baseline sufficient to allow for occasional recombination.

718

719 *Protein structure analysis*

720 VMD was used to visualize the protein structures and analyze the potential functional effects of
721 mutations (Humphrey et al. 1996). Figure 3 was created using Inkscape (https://inskape.org/)
722 and Gimp 2.8 (https://www.gimp.org) (Anon).

723

724 *Molecular dynamics simulations*

725 Molecular dynamics (MD) simulations were used to study interactions between SARS-CoV-2
726 RBD and ACE2 from ferret and human. Three independent extensive MD simulations were
727 performed for each species using GROMACS 2020 package (Lindahl et al. 2020) and the
728 CHARMM36 force field for protein and glycans (Guvench et al. 2011; Huang and MacKerell
729 2013). Each simulation ran up to 800 ns, being the last 500 ns used for analysis. PDB id 6M17
730 was used to build the ACE2-RBD complexes. Given the high sequence identity between human
731 and ferret ACE2 (83%), we performed local modeling of the non-conserved amino acid residues
732 in ferret ACE2 using the human homolog as the template, via RosettaRemodel (Huang et al.
733 2011).

734 The inputs for simulations were generated using CHARMM-GUI (Jo et al. 2008).
735 Counterions were added for electroneutrality (0.1 M NaCl). The complexes were surrounded by
736 TIP3P water molecules to form a layer of at least 10 Å relative to the box borders (Jorgensen et
737 al. 1983). Simulations were performed using the NPT ensemble. The temperature was
738 maintained at 310 K with the Nosé–Hoover thermostat using a time constant of 1.0 ps (Evans
739 and Holian 1985). The pressure was maintained at 1 bar with the isotropic Parrinello–Rahman
740 barostat using a compressibility of 4.5×10^{-5} bar^{-1} and a time constant of 1.0 ps in a rectangular
741 simulation box (Parrinello and Rahman 1981). The particle mesh Ewald method was used for the

742 treatment of periodic electrostatic interactions with a cutoff distance of 1.2 nm (Darden et al.
743 1993). The Lennard–Jones potential was smoothed over the cutoff range of 1.0–1.2 nm by using
744 the force-based switching function. Only atoms in the Verlet pair list with a cutoff range
745 reassigned every 20 steps were considered. The LINCS algorithm was used to constrain all
746 bonds involving hydrogen atoms to allow the use of a 2 fs time step (Hess et al. 1997). The
747 suggested protocol for nonbonded interactions with the CHARMM36 force field when used in
748 the GROMACS suite was followed.

749 The Hbonds plugin in VMD was used to identify hydrogen bond interactions along the
750 simulations (Humphrey et al. 1996). The geometric criteria adopted are a cutoff of 3.5 Å for
751 donor-acceptor distance and 30° for acceptor-donor-H angle. The Timeline plugin was used to
752 count contacts formed by a given amino acid residue. We defined the distance of 4 Å between
753 any atom pairs as the cutoff for contact.

754

755 **5. Data Access**

756 All SARS-CoV-2 sequences used in this study are available from the public repositories Genome
757 Initiative on Sharing Avian Influenza Data (GISAID, gisaid.org), the National Center for
758 Biotechnology Information (NCBI, https://www.ncbi.nlm.nih.gov/sars-cov-2/) and the COVID-19
759 Genomics UK Consortium (COG, https://www.sanger.ac.uk/collaboration/covid-19-genomics-
760 uk-cog-uk-consortium/

761

762 ***6.* Acknowledgments**

763 The viral evolution research was funded by the Laboratory Directed Research and Development
764 Program of Oak Ridge National Laboratory, managed by UT-Battelle, LLC for the US
765 Department of Energy (LOIS:10074) and the structural implication work was funded via the
766 DOE Office of Science through the National Virtual Biotechnology Laboratory (NVBL), a
767 consortium of DOE national laboratories focused on the response to COVID-19, with funding
768 provided by the Coronavirus CARES Act. This work was also funded by the United States
769 Government. This research used resources of the Oak Ridge Leadership Computing Facility
770 (OLCF) and the Compute and Data Environment for Science (CADES) at the Oak Ridge
771 National Laboratory, which is supported by the Office of Science of the U.S. Department of
772 Energy under Contract No. DE-AC05-00OR22725. Figures generated with Biorender and
773 VMD. We gratefully acknowledge the Originating laboratories responsible for obtaining the

viral specimens and the Submitting laboratories where genetic sequence data were generated and shared via the GISAID Initiative, on which this research is based.

Author Contribution

MR Garvin: Conceptualization, Data curation, Funding acquisition, Formal Analysis, Investigation, Methodology, Visualization, Writing – original draft, Writing – review & editing.

ET Prates: Formal Analysis, Investigation, Visualization, Writing - original draft, Writing - review & editing

J Romero: Conceptualization, Formal Analysis, Investigation, Methodology, Software, Writing – original draft, Writing – review & editing.

A Cliff: Methodology, Software, Writing – review & editing

JGFM Gazolla: Software, Formal Analysis, Investigation, Data Curation, Visualization, Writing - Review and Editing.

M Pickholz: Investigation, Visualization, Writing – original draft, Writing – review & editing

M Pavicic: Investigation, Writing – original draft, Writing – review & editing

DA Jacobson: Conceptualization, Funding acquisition, Formal Analysis, Investigation, Project administration, Supervision, Resources, Writing – original draft, Writing – review & editing

792 **7. References**

793 Ali A, Vijayan R. 2020. Dynamics of the ACE2-SARS-CoV-2/SARS-CoV spike protein
794 interface reveal unique mechanisms. *Sci. Rep.* 10:14214.

795 Alpert T, Brito AF, Lasek-Nesselquist E, Rothman J, Valesano AL, MacKay MJ, Petrone ME,
796 Breban MI, Watkins AE, Vogels CBF, et al. 2021. Early introductions and transmission of
797 SARS-CoV-2 variant B.1.1.7 in the United States. *Cell* 184:2595–2604.e13.

798 Anisimova M, Nielsen R, Yang Z. 2003. Effect of recombination on the accuracy of the
799 likelihood method for detecting positive selection at amino acid sites. *Genetics* 164:1229–
800 1236.

801 Anon. The GIMP Development Team. (2019). GIMP. Retrieved from https://www.gimp.org.
802 *https://www.gimp.org*.

803 Bandelt HJ, Forster P, Röhl A. 1999. Median-joining networks for inferring intraspecific
804 phylogenies. *Mol. Biol. Evol.* 16:37–48.

805 Bentley K, Evans DJ. 2018. Mechanisms and consequences of positive-strand RNA virus
806 recombination. *J. Gen. Virol.* 99:1345–1356.

807 Boni MF, Lemey P, Jiang X, Lam TT-Y, Perry BW, Castoe TA, Rambaut A, Robertson DL.
808 2020. Evolutionary origins of the SARS-CoV-2 sarbecovirus lineage responsible for the
809 COVID-19 pandemic. *Nat Microbiol* 5:1408–1417.

810 Calistri P, Amato L, Puglia I, Cito F, Di Giuseppe A, Danzetta ML, Morelli D, Di Domenico M,
811 Caporale M, Scialabba S, et al. 2021. Infection sustained by lineage B.1.1.7 of SARS-CoV-
812 2 is characterised by longer persistence and higher viral RNA loads in nasopharyngeal
813 swabs. *Int. J. Infect. Dis.* 105:753–755.

814 Casalino L, Gaieb Z, Goldsmith JA, Hjorth CK, Dommer AC, Harbison AM, Fogarty CA,
815 Barros EP, Taylor BC, McLellan JS, et al. 2020. Beyond Shielding: The Roles of Glycans
816 in the SARS-CoV-2 Spike Protein. *ACS Cent Sci* 6:1722–1734.

817 Challen R, Brooks-Pollock E, Read JM, Dyson L, Tsaneva-Atanasova K, Danon L. 2021. Risk
818 of mortality in patients infected with SARS-CoV-2 variant of concern 202012/1: matched
819 cohort study. *BMJ* 372:n579.

820 Chen J, Malone B, Llewellyn E, Grasso M, Shelton PMM, Olinares PDB, Maruthi K, Eng ET,
821 Vatandaslar H, Chait BT, et al. 2020. Structural Basis for Helicase-Polymerase Coupling in
822 the SARS-CoV-2 Replication-Transcription Complex. *Cell* 182:1560–1573.e13.

823 Darden T, York D, Pedersen L. 1993. Particle mesh Ewald: An N·log(N) method for Ewald sums
824 in large systems. *J. Chem. Phys.* 98:10089–10092.

825 Davies NG, Jarvis CI, John Edmunds W, Jewell NP, Diaz-Ordaz K, Keogh RH, CMMID
826 COVID-19 Working Group. Increased mortality in community-tested cases of SARS-CoV-
827 2 lineage B.1.1.7. Available from: http://dx.doi.org/10.1101/2021.02.01.21250959

828 Deng X, Garcia-Knight MA, Khalid MM, Servellita V, Wang C, Morris MK, Sotomayor-
829 González A, Glasner DR, Reyes KR, Gliwa AS, et al. 2021. Transmission, infectivity, and
830 neutralization of a spike L452R SARS-CoV-2 variant. *Cell* 184:3426–3437.e8.

831 Dutta NK, Mazumdar K, Gordy JT. 2020. The Nucleocapsid Protein of SARS–CoV-2: a Target
832 for Vaccine Development. *Journal of Virology* [Internet] 94. Available from:
833 http://dx.doi.org/10.1128/jvi.00647-20

834 Evans DJ, Holian BL. 1985. The Nose–Hoover thermostat. *J. Chem. Phys.* 83:4069–4074.

835 Faria NR, Mellan TA, Whittaker C, Claro IM, Candido D da S, Mishra S, Crispim MAE, Sales
836 FCS, Hawryluk I, McCrone JT, et al. 2021. Genomics and epidemiology of the P.1 SARS-
837 CoV-2 lineage in Manaus, Brazil. *Science* 372:815–821.

838 Fratev F. The N501Y and K417N mutations in the spike protein of SARS-CoV-2 alter the
839 interactions with both hACE2 and human derived antibody: A Free energy of perturbation
840 study. Available from: http://dx.doi.org/10.1101/2020.12.23.424283

841 Funk T, Pharris A, Spiteri G, Bundle N, Melidou A, Carr M, Gonzalez G, Garcia-Leon A,
842 Crispie F, O'Connor L, et al. 2021. Characteristics of SARS-CoV-2 variants of concern

843 B.1.1.7, B.1.351 or P.1: data from seven EU/EEA countries, weeks 38/2020 to 10/2021.
844 *Euro Surveill.* [Internet] 26. Available from: http://dx.doi.org/10.2807/1560-
845 7917.ES.2021.26.16.2100348

846 Garvin MR, Prates ET, Pavicic M, Jones P, Amos BK, Geiger A, Shah M, Streich J, Gazolla
847 JGFM, Kainer D, et al. 2020. Potentially adaptive SARS-CoV-2 mutations discovered with
848 novel spatiotemporal and explainable-AI models. *Genome Biol.* in press.

849 Garvin MR, T Prates E, Pavicic M, Jones P, Amos BK, Geiger A, Shah MB, Streich J, Felipe
850 Machado Gazolla JG, Kainer D, et al. 2020. Potentially adaptive SARS-CoV-2 mutations
851 discovered with novel spatiotemporal and explainable AI models. *Genome Biol.* 21:304.

852 Greaney AJ, Starr TN, Gilchuk P, Zost SJ, Binshtein E, Loes AN, Hilton SK, Huddleston J,
853 Eguia R, Crawford KHD, et al. Complete mapping of mutations to the SARS-CoV-2 spike
854 receptor-binding domain that escape antibody recognition. Available from:
855 http://dx.doi.org/10.1101/2020.09.10.292078

856 Gribble J, Stevens LJ, Agostini ML, Anderson-Daniels J, Chappell JD, Lu X, Pruijssers AJ,
857 Routh AL, Denison MR. 2021. The coronavirus proofreading exoribonuclease mediates
858 extensive viral recombination. *PLoS Pathog.* 17:e1009226.

859 Gu H, Chen Q, Yang G, He L, Fan H, Deng Y-Q, Wang Y, Teng Y, Zhao Z, Cui Y, et al. 2020.
860 Adaptation of SARS-CoV-2 in BALB/c mice for testing vaccine efficacy. *Science*
861 369:1603–1607.

862 Guo G, Gao M, Gao X, Zhu B, Huang J, Luo K, Zhang Y, Sun J, Deng M, Lou Z. 2021. SARS-
863 CoV-2 non-structural protein 13 (nsp13) hijacks host deubiquitinase USP13 and counteracts
864 host antiviral immune response. *Signal Transduct Target Ther* 6:119.

865 Gupta R, Charron J, Stenger CL, Painter J, Steward H, Cook TW, Faber W, Frisch A, Lind E,
866 Bauss J, et al. 2020. SARS-CoV-2 (COVID-19) structural and evolutionary dynamicome:
867 Insights into functional evolution and human genomics. *J. Biol. Chem.* 295:11742–11753.

868 Guvench O, Mallajosyula SS, Raman EP, Hatcher E, Vanommeslaeghe K, Foster TJ, Jamison
869 FW 2nd, Mackerell AD Jr. 2011. CHARMM additive all-atom force field for carbohydrate

870 derivatives and its utility in polysaccharide and carbohydrate-protein modeling. *J. Chem.*
871 *Theory Comput.* 7:3162–3180.

872 Hess B, Bekker H, Berendsen HJC, Fraaije JGEM. 1997. LINCS: A linear constraint solver for
873 molecular simulations. *J. Comput. Chem.* 18:1463–1472.

874 Hoffmann M, Kleine-Weber H, Pöhlmann S. 2020. A Multibasic Cleavage Site in the Spike
875 Protein of SARS-CoV-2 Is Essential for Infection of Human Lung Cells. *Mol. Cell* 78:779–
876 784.e5.

877 Huang J, MacKerell AD Jr. 2013. CHARMM36 all-atom additive protein force field: validation
878 based on comparison to NMR data. *J. Comput. Chem.* 34:2135–2145.

879 Huang P-S, Ban Y-EA, Richter F, Andre I, Vernon R, Schief WR, Baker D. 2011.
880 RosettaRemodel: a generalized framework for flexible backbone protein design. *PLoS One*
881 6:e24109.

882 Humphrey W, Dalke A, Schulten K. 1996. VMD: visual molecular dynamics. *J. Mol. Graph.*
883 14:33–38, 27–28.

884 Huson DH, Bryant D. 2006. Application of phylogenetic networks in evolutionary studies. *Mol.*
885 *Biol. Evol.* 23:254–267.

886 Jang K-J, Jeong S, Kang DY, Sp N, Yang YM, Kim D-E. 2020. A high ATP concentration
887 enhances the cooperative translocation of the SARS coronavirus helicase nsP13 in the
888 unwinding of duplex RNA. *Sci. Rep.* 10:4481.

889 Jia Z, Yan L, Ren Z, Wu L, Wang J, Guo J, Zheng L, Ming Z, Zhang L, Lou Z, et al. 2019.
890 Delicate structural coordination of the Severe Acute Respiratory Syndrome coronavirus
891 Nsp13 upon ATP hydrolysis. *Nucleic Acids Res.* 47:6538–6550.

892 Jorgensen WL, Chandrasekhar J, Madura JD, Impey RW, Klein ML. 1983. Comparison of
893 simple potential functions for simulating liquid water. *J. Chem. Phys.* 79:926–935.

894 Jo S, Kim T, Iyer VG, Im W. 2008. CHARMM-GUI: a web-based graphical user interface for

895 CHARMM. *J. Comput. Chem.* 29:1859–1865.

896 Jumper J, Tunyasuvunakool K, Kohli P, Hassabis D, AlphaFold Team. Computational
897 predictions of protein structures associated with COVID-19. *Deep Mind* [Internet].
898 Available from: https://deepmind.com/research/open-source/computational-predictions-of-
899 protein-structures-associated-with-COVID-19

900 Katoh K, Misawa K, Kuma K-I, Miyata T. 2002. MAFFT: a novel method for rapid multiple
901 sequence alignment based on fast Fourier transform. *Nucleic Acids Res.* 30:3059–3066.

902 Kim D, Lee J-Y, Yang J-S, Kim JW, Kim VN, Chang H. 2020. The Architecture of SARS-CoV-
903 2 Transcriptome. *Cell* 181:914–921.e10.

904 Korber B, Fischer WM, Gnanakaran S, Yoon H, Theiler J, Abfalterer W, Hengartner N, Giorgi
905 EE, Bhattacharya T, Foley B, et al. 2020. Tracking Changes in SARS-CoV-2 Spike:
906 Evidence that D614G Increases Infectivity of the COVID-19 Virus. *Cell* 182:812–827.e19.

907 Lauring AS, Hodcroft EB. 2021. Genetic Variants of SARS-CoV-2-What Do They Mean? *JAMA*
908 325:529–531.

909 Leigh JW, Bryant D. 2015. popart: full-feature software for haplotype network construction.
910 *Methods Ecol. Evol.* 6:1110–1116.

911 Lindahl, Abraham, Hess, Spoel V der. 2020. GROMACS 2020 Source code. Available from:
912 https://zenodo.org/record/3562495

913 Liu Y, Liu J, Plante KS, Plante JA, Xie X, Zhang X, Ku Z, An Z, Scharton D, Schindewolf C, et
914 al. 2021. The N501Y spike substitution enhances SARS-CoV-2 transmission. *bioRxiv*
915 [Internet]. Available from: http://dx.doi.org/10.1101/2021.03.08.434499

916 Li Y, Ma M-L, Lei Q, Wang F, Hong W, Lai D-Y, Hou H, Xu Z-W, Zhang B, Chen H, et al.
917 2021. Linear epitope landscape of the SARS-CoV-2 Spike protein constructed from 1,051
918 COVID-19 patients. *Cell Rep.* 34:108915.

919 Luan B, Wang H, Huynh T. Molecular Mechanism of the N501Y Mutation for Enhanced

920 Binding between SARS-CoV-2's Spike Protein and Human ACE2 Receptor. Available
921 from: http://dx.doi.org/10.1101/2021.01.04.425316

922 Lu J, Li B, Deng A, Li K, Hu Y, Li Z, Xiong Q, Liu Z, Guo Q, Zou L, et al. Viral infection and
923 transmission in a large, well-traced outbreak caused by the SARS-CoV-2 Delta variant.
924 Available from: http://dx.doi.org/10.21203/rs.3.rs-738164/v1

925 Martin DP, Weaver S, Tegally H, San EJ, Shank SD, Wilkinson E, Giandhari J, Naidoo S, Pillay
926 Y, Singh L, et al. 2021. The emergence and ongoing convergent evolution of the N501Y
927 lineages coincides with a major global shift in the SARS-CoV-2 selective landscape.
928 *medRxiv* [Internet]. Available from: http://dx.doi.org/10.1101/2021.02.23.21252268

929 Muller HJ. 1964. THE RELATION OF RECOMBINATION TO MUTATIONAL ADVANCE.
930 *Mutat. Res.* 106:2–9.

931 Oude Munnink BB, Sikkema RS, Nieuwenhuijse DF, Molenaar RJ, Munger E, Molenkamp R,
932 van der Spek A, Tolsma P, Rietveld A, Brouwer M, et al. 2021. Transmission of SARS-
933 CoV-2 on mink farms between humans and mink and back to humans. *Science* 371:172–
934 177.

935 Papa G, Mallery DL, Albecka A, Welch L, Cattin-Ortolá J, Luptak J, Paul D, McMahon HT,
936 Goodfellow IG, Carter A, et al. Furin cleavage of SARS-CoV-2 Spike promotes but is not
937 essential for infection and cell-cell fusion. Available from:
938 http://dx.doi.org/10.1101/2020.08.13.243303

939 Parrinello M, Rahman A. 1981. Polymorphic transitions in single crystals: A new molecular
940 dynamics method. *J. Appl. Phys.* 52:7182–7190.

941 Prates E, Garvin M, Jones P, Miller JI, Kyle S, Cliff A, Gazolla JGFM, Shah M, Walker A, Lane
942 M, et al. 2021. Antiviral Strategies Against SARS-CoV-2 – For a Bioinformatics Approach.
943 In: Hann JJ, Bintou A, Keng C, editors. SARS-CoV-2 Methods and Protocols. Spriinger.

944 Prates ET, Garvin MR, Pavicic M, Jones P, Shah M, Demerdash O, Amos BK, Geiger A,
945 Jacobson D. 2020. Potential pathogenicity determinants identified from structural
946 proteomics of SARS-CoV and SARS-CoV-2. *Mol. Biol. Evol.* [Internet]. Available from:

947 http://dx.doi.org/10.1093/molbev/msaa231

948 Rand AC, Jain M, Eizenga JM, Musselman-Brown A, Olsen HE, Akeson M, Paten B. 2017.
949 Mapping DNA methylation with high-throughput nanopore sequencing. *Nat. Methods*
950 14:411–413.

951 Richard M, Kok A, de Meulder D, Bestebroer TM, Lamers MM, Okba NMA, Fentener van
952 Vlissingen M, Rockx B, Haagmans BL, Koopmans MPG, et al. 2020. SARS-CoV-2 is
953 transmitted via contact and via the air between ferrets. *Nat. Commun.* 11:3496.

954 Rodrigues CHM, Pires DEV, Ascher DB. 2021. DynaMut2: Assessing changes in stability and
955 flexibility upon single and multiple point missense mutations. *Protein Sci.* 30:60–69.

956 Ronquist F, Huelsenbeck JP. 2003. MrBayes 3: Bayesian phylogenetic inference under mixed
957 models. *Bioinformatics* 19:1572–1574.

958 Sabino EC, Buss LF, Carvalho MPS, Prete CA Jr, Crispim MAE, Fraiji NA, Pereira RHM, Parag
959 KV, da Silva Peixoto P, Kraemer MUG, et al. 2021. Resurgence of COVID-19 in Manaus,
960 Brazil, despite high seroprevalence. *Lancet* [Internet]. Available from:
961 http://dx.doi.org/10.1016/S0140-6736(21)00183-5

962 Santerre M, Arjona SP, Allen CN, Shcherbik N, Sawaya BE. 2020. Why do SARS-CoV-2 NSPs
963 rush to the ER? *J. Neurol.* [Internet]. Available from: http://dx.doi.org/10.1007/s00415-020-
964 10197-8

965 Sawatzki K, Hill NJ, Puryear WB, Foss AD, Stone JJ, Runstadler JA. 2021. Host barriers to
966 SARS-CoV-2 demonstrated by ferrets in a high-exposure domestic setting. *Proc. Natl.*
967 *Acad. Sci. U. S. A.* [Internet] 118. Available from:
968 http://dx.doi.org/10.1073/pnas.2025601118

969 Shang J, Ye G, Shi K, Wan Y, Luo C, Aihara H, Geng Q, Auerbach A, Li F. 2020. Structural
970 basis of receptor recognition by SARS-CoV-2. *Nature* 581:221–224.

971 Shannon P, Markiel A, Ozier O, Baliga NS, Wang JT, Ramage D, Amin N, Schwikowski B,
972 Ideker T. 2003. Cytoscape: a software environment for integrated models of biomolecular

973 interaction networks. *Genome Res.* 13:2498–2504.

974 Sheikh A, McMenamin J, Taylor B, Robertson C. 2021. SARS-CoV-2 Delta VOC in Scotland:
975 demographics, risk of hospital admission, and vaccine effectiveness. *The Lancet* [Internet].
976 Available from: http://dx.doi.org/10.1016/s0140-6736(21)01358-1

977 Simon-Loriere E, Holmes EC. 2011. Why do RNA viruses recombine? *Nat. Rev. Microbiol.*
978 9:617–626.

979 Simpson JT, Workman RE, Zuzarte PC, David M, Dursi LJ, Timp W. 2017. Detecting DNA
980 cytosine methylation using nanopore sequencing. *Nat. Methods* 14:407–410.

981 Singh A, Steinkellner G, Köchl K, Gruber K, Gruber CC. Serine 477 plays a crucial role in the
982 interaction of the SARS-CoV-2 spike protein with the human receptor ACE2. Available
983 from: http://dx.doi.org/10.21203/rs.3.rs-106969/v1

984 Singh J, Rahman SA, Ehtesham NZ, Hira S, Hasnain SE. 2021. SARS-CoV-2 variants of
985 concern are emerging in India. *Nat. Med.* [Internet]. Available from:
986 http://dx.doi.org/10.1038/s41591-021-01397-4

987 Starr TN, Greaney AJ, Addetia A, Hannon WW, Choudhary MC, Dingens AS, Li JZ, Bloom JD.
988 2021. Prospective mapping of viral mutations that escape antibodies used to treat COVID-
989 19. *Science* [Internet]. Available from: http://dx.doi.org/10.1126/science.abf9302

990 Starr TN, Greaney AJ, Hilton SK, Crawford KHD, Navarro MJ, Bowen JE, Alejandra Tortorici
991 M, Walls AC, Veesler D, Bloom JD. Deep mutational scanning of SARS-CoV-2 receptor
992 binding domain reveals constraints on folding and ACE2 binding. Available from:
993 http://dx.doi.org/10.1101/2020.06.17.157982

994 Thorne LG, Bouhaddou M, Reuschl A-K, Zuliani-Alvarez L, Polacco B, Pelin A, Batra J,
995 Whelan MVX, Ummadi M, Rojc A, et al. 2021. Evolution of enhanced innate immune
996 evasion by the SARS-CoV-2 B.1.1.7 UK variant. *bioRxiv* [Internet]. Available from:
997 http://dx.doi.org/10.1101/2021.06.06.446826

998 Tylor S, Andonov A, Cutts T, Cao J, Grudesky E, Van Domselaar G, Li X, He R. 2009. The SR-

999 rich motif in SARS-CoV nucleocapsid protein is important for virus replication. *Canadian*
1000 *Journal of Microbiology* [Internet] 55:254–260. Available from:
1001 http://dx.doi.org/10.1139/w08-139

1002 Velasco JD. 2013. Phylogeny as population history. *Philosophy and Theory in Biology* [Internet]
1003 5. Available from: http://dx.doi.org/10.3998/ptb.6959004.0005.002

1004 Verba K, Gupta M, Azumaya C, Moritz M, Pourmal S, Diallo A, Merz G, Jang G, Bouhaddou
1005 M, Fossati A, et al. 2021. CryoEM and AI reveal a structure of SARS-CoV-2 Nsp2, a
1006 multifunctional protein involved in key host processes. *Res Sq* [Internet]. Available from:
1007 http://dx.doi.org/10.21203/rs.3.rs-515215/v1

1008 Volz E, Mishra S, Chand M, Barrett JC, Johnson R, Geidelberg L, Hinsley WR, Laydon DJ,
1009 Dabrera G, O'Toole Á, et al. Transmission of SARS-CoV-2 Lineage B.1.1.7 in England:
1010 Insights from linking epidemiological and genetic data. Available from:
1011 http://dx.doi.org/10.1101/2020.12.30.20249034

1012 Wang Z, Schmidt F, Weisblum Y, Muecksch F, Barnes CO, Finkin S, Schaefer-Babajew D,
1013 Cipolla M, Gaebler C, Lieberman JA, et al. 2021. mRNA vaccine-elicited antibodies to
1014 SARS-CoV-2 and circulating variants. *Nature* [Internet]. Available from:
1015 http://dx.doi.org/10.1038/s41586-021-03324-6

1016 Washington NL, Gangavarapu K, Zeller M, Bolze A, Cirulli ET, Schiabor Barrett KM, Larsen
1017 BB, Anderson C, White S, Cassens T, et al. 2021. Emergence and rapid transmission of
1018 SARS-CoV-2 B.1.1.7 in the United States. *Cell* 184:2587–2594.e7.

1019 Wrapp D, Wang N, Corbett KS, Goldsmith JA, Hsieh C-L, Abiona O, Graham BS, McLellan JS.
1020 2020. Cryo-EM structure of the 2019-nCoV spike in the prefusion conformation. *Science*
1021 367:1260–1263.

1022 Xia H, Cao Z, Xie X, Zhang X, Chen JY-C, Wang H, Menachery VD, Rajsbaum R, Shi P-Y.
1023 2020. Evasion of Type I Interferon by SARS-CoV-2. *Cell Rep.* 33:108234.

1024 Yan L, Zhang Y, Ge J, Zheng L, Gao Y, Wang T, Jia Z, Wang H, Huang Y, Li M, et al. 2020.
1025 Architecture of a SARS-CoV-2 mini replication and transcription complex. *Nat. Commun.*

1026 11:5874.

1027 Yan R, Zhang Y, Li Y, Xia L, Guo Y, Zhou Q. 2020. Structural basis for the recognition of
1028 SARS-CoV-2 by full-length human ACE2. *Science* 367:1444–1448.

1029 Zhang B-Z, Hu Y-F, Chen L-L, Yau T, Tong Y-G, Hu J-C, Cai J-P, Chan K-H, Dou Y, Deng J,
1030 et al. 2020. Mining of epitopes on spike protein of SARS-CoV-2 from COVID-19 patients.
1031 *Cell Res.* 30:702–704.

1032 Zhang L, Jackson CB, Mou H, Ojha A, Peng H, Quinlan BD, Rangarajan ES, Pan A,
1033 Vanderheiden A, Suthar MS, et al. 2020. SARS-CoV-2 spike-protein D614G mutation
1034 increases virion spike density and infectivity. *Nat. Commun.* 11:6013.